Comparison of fluid and kinetic models of target energy fluxes during edge localized modes

2012 Plasma Phys. Control. Fusion 54 045002

(http://iopscience.iop.org/0741-3335/54/4/045002)

Plasma Phys. Control. Fusion **54** (2012) 045002 (21pp) doi:10.1088/0741-3335/54/4/045002

Comparison of fluid and kinetic models of target energy fluxes during edge localized modes

E Havlíčková[1], W Fundamenski[1], D Tskhakaya[2,4], G Manfredi[3] and D Moulton[1]

[1] EURATOM/CCFE Fusion Association, Culham Science Centre, Abingdon, Oxon, OX14 3DB, UK
[2] Association EURATOM-ÖAW, Institute of Theoretical Physics, University of Innsbruck, A-6020 Innsbruck, Austria
[3] Institut de Physique et Chimie des Matériaux, CNRS and Université de Strasbourg, BP 43, F-67034 Strasbourg, France

E-mail: eva.havlickova@ccfe.ac.uk

Received 7 November 2011, in final form 26 January 2012
Published 14 March 2012
Online at stacks.iop.org/PPCF/54/045002

Abstract
Parallel transport associated with type I edge localized model (ELM) filaments in the scrape-off layer (SOL) is studied by means of three computational approaches—fluid, Vlasov and particle-in-cell (PIC). These techniques are benchmarked for convective transients by analysing power fluxes at the target. In spite of kinetic effects due to fast electrons which are not captured in the fluid code, the overall agreement between the codes is satisfactory. In addition, the collisionless Vlasov model agrees well with an analytic free-streaming model. The total peak energy flux at the target is comparable between the models, but the individual fractions of the flux carried by ion and electron components are determined by kinetic effects and processes in the sheath and the energy source in the fluid code is redistributed between electrons and ions in order to obtain the best match with the PIC model. From results for convective ELMs, approximate expressions for the energy fluence and the peak energy flux at the target are derived. Additionally, conductive ELMs are studied.

(Some figures may appear in colour only in the online journal)

1. Introduction

Transient behaviour of plasma is found in the scrape-off layer (SOL) both in L-mode regimes where dynamics is dominated by turbulence and in H-mode regimes which are accompanied by quasi-periodic edge localized modes (ELMs). Description of dynamic effects in the SOL requires time-dependent modelling opposed to more standard laminar models using time-averaged plasma quantities [1]. In this study, parallel transient transport in the SOL is investigated in response of type I ELMs.

ELMs are MHD instabilities associated with H-mode confinement and occurrence of steep pedestal gradients, resulting in a collapse of the pedestal and transient ejection of plasma from the pedestal region into the SOL. Investigated type I ELMs can expel up to 10% of stored plasma energy which is then transported towards the wall and divertor targets. Subsequent increase in incident power and particle loads on plasma facing components (PFCs) has crucial consequences for the design of future devices. To avoid degradation of PFCs and reduction of their life times due to erosion and melting, it is necessary to limit the peak and total power loads deposited on divertor targets below a tolerable maximum. Moreover, the main chamber wall is affected by the interaction with ELMs which leads to increased impurity content and their eventual penetration into the core. Typically, predictions of deposited power for future devices are made by extrapolation of experimental results from present-day tokamaks [3–5]. Alternatively, the amount of power transferred to the targets can be estimated from numerical models. In JET experiments, type I ELMs are typically depositing energies of 5–80 kJ m^{-2} with corresponding peak power loads 40–120 MW m^{-2} on divertor plates [4–6]. These values will be much higher in

[4] Permanent address: Andronikashvili Institute of Physics, 0177 Tbilisi, Georgia.

ITER and the material limit estimated for ITER is 0.5 MJ m^{-2} per ELM (500 μs) as stated in [4].

The physical mechanism of the ELM cycle is not yet fully explained and its investigation involves more complex MHD physics and development of new theories. However, without addressing the origin and driving mechanism of these events in the pedestal, dynamics in the SOL during the ELM crash can be modelled by SOL transport codes used in the time-dependent fashion. In two-dimensional codes, radial transport is amplified for the period of the ELM crash by increasing radial diffusivities [2]. In one dimension, the sources representing released ELM particles and energy from the pedestal into the SOL must be prescribed. Predictions of target power loads can then be obtained from energy balance in the SOL.

High temperatures in the pedestal resulting in very low collisionalities present evidence of the kinetic nature of ELMs. It is generally thought that kinetic effects play an important role in the description of low-collisionality transients and kinetic treatment of their dynamics in the SOL is required. On the other hand, fluid models are extensively used as SOL transport solvers, namely two-dimensional multi-fluid codes such as EDGE2D or SOLPS which are widely used to interpret experiments, guide design of devices and make predictions for future machines. Kinetic effects cannot be resolved in the fluid treatment, although it is possible to introduce kinetic corrections on the macroscopic level, e.g. modifying transport coefficient (in the form of flux limiting factors) or boundary conditions. This is guided by comparison of fluid and kinetic results. In the past, the present-day SOL transport codes encountered difficulties when modelling ELM filaments [7]. Moreover, they are commonly used in steady-state and only recent work is devoted to transients [2, 7–9]. Kinetic treatment was used, e.g., in [10] or more recently in [3, 11] where parallel transport in the JET SOL associated with type I ELMs has been studied numerically by the BIT1 code and results were successfully compared with experiment [12].

The objective of this study is to benchmark one-dimensional codes based on particle-in-cell (PIC) method (BIT1 code), Vlasov model and fluid model (SOLF1D code) for simulating plasma transport parallel to the magnetic field during the ELM crash of purely convective ELMs. We benchmark the models by analysing target energy fluxes, in order to compare the peak and total power loads on the target and identify which features of parallel dynamics can be described by the fluid technique and where the fluid codes are likely to fail. An analytic free-streaming description is also examined. Approximate fits for the peak energy flux at the target and the total deposited energy during the transient in terms of pedestal parameters are constructed from results of the one-dimensional codes for JET and used with the density and temperature expected on ITER.

2. Description of models

2.1. BIT1 code

BIT1 is an electrostatic PIC Monte Carlo code for one-dimensional simulations of plasma edge [13]. Code follows plasma, neutral and impurity particles. Particle trajectories are calculated according to

$$\frac{\mathrm{d}\boldsymbol{v}}{\mathrm{d}t} = \frac{e}{m}(\boldsymbol{E} + \boldsymbol{v} \times \boldsymbol{B}) + st \tag{1}$$

where e and m are particle charge and mass and st is the collision term, taking into account the elastic and inelastic collisions between particles and the interaction with the divertor plates. Coulomb collisions are treated via optimized binary collision model [14], while charge–neutral and neutral–neutral particle collisions are modelled via non-linear null collision method [15]. All collision operations conserve momentum and energy. The plasma–surface interaction model is linear with prescribed secondary electron emission, plasma recycling and impurity sputtering coefficients [16]. All these coefficients depend on the energy and the incidence angle of particles impinging on the divertor plates. The electric field is obtained from the Poisson equation and the magnetic field is fixed. The simulations presented here were performed via serial version of the BIT1 code and correspond to the simplified model without neutral and impurity particles. The simulation region corresponds to the one-dimensional SOL with particle source in the middle of the system. During the simulations, the finest time and space scales are resolved (down to the particle gyro-rotation and plasma oscillation). Further details can be found in [13].

Simulations of the BIT1 code published in [3] represent a baseline for this study. A series of simulations of parallel transport during ELMs in the JET tokamak was performed and a comparison with experiment was also provided, showing sensivity to impurities and recycling [11, 12].

Recent studies also focused on the behaviour of kinetic factors during transients, such as heat flux and viscosity limiters and sheath energy transmission coefficients, proving their complex and strong variations both in time and space [12, 16, 17].

2.2. Vlasov code

The second modelling approach examined here is based on the Vlasov equation [18]. We adopt a one-dimensional geometry along the parallel direction, here denoted x, with corresponding parallel velocity $v_\parallel$. In the perpendicular plane, the distribution function remains Maxwellian at all times, so that the distribution in the four-dimensional phase space $(x, \boldsymbol{v})$ reads as $F_j(x, \boldsymbol{v}, t) = f_j(x, v_\parallel, t) M_{\perp,j}(\boldsymbol{v}_\perp)$, where $M_{\perp,j}(\boldsymbol{v}_\perp) = (m_j/2\pi T_{\mathrm{ped}}) \exp(-m_j v_\perp^2/2T_{\mathrm{ped}})$, T_{ped} is the pedestal temperature and the label $j = \mathrm{i}, \mathrm{e}$ stands for ions and electrons, respectively.

Under these assumptions, the ion and electron evolutions are described by the one-dimensional Vlasov equations for the parallel distribution functions $f_j(x, v_\parallel, t)$

$$\frac{\partial f_j}{\partial t} + v_\parallel \frac{\partial f_j}{\partial x} - \frac{q_j}{m_j}\frac{\partial \phi}{\partial x}\frac{\partial f_j}{\partial v_\parallel} = g(t) S(x) M_{\parallel,j}(v_\parallel) \tag{2}$$

where $q_j = \pm e$. This collisionless approximation is reasonable for the initial phase of high-energy transients such

as ELMs, for which the thermal mean-free-path exceeds the parallel connection length.

In the source term on the right-hand side of equation (2), $g(t)$ models the pulse temporal profile, $S(x)$ is the spatial profile of the source, and $M_{\parallel,j}$ is a Maxwellian distribution in the parallel velocity. Finally, the electrostatic potential $\phi(x,t)$ is computed self-consistently from the one-dimensional Poisson equation.

The Vlasov equation (2) is solved using an Eulerian method based on a uniform meshing of the parallel phase space $(x, v_\parallel)$. For the time-stepping, a second-order splitting scheme is used, which solves alternatively the advection in real space and the advection in velocity space. Each advection step is performed using a third-order positive flux-conservative method, with a slope corrector that prevents the distribution function from becoming negative [19].

In addition, a recently developed 'asymptotic-preserving' numerical scheme [20] allowed us to lift numerical constraints on the time step and grid spacing, which are no longer limited by, respectively, the electron plasma period and Debye length. Typical resolution of the code is $N_x = 4000$ and $N_v = 1000$ grid points in real and velocity space and the time step is $\Delta t = 0.001\tau_\parallel^{\mathrm{e}}$, where $\tau_\parallel^{\mathrm{e}}$ is the electron transit time. One calculation takes about 15 h on a standard PC.

2.3. SOLF1D code

The SOLF1D model is based on the one-dimensional Braginskii equations for the plasma density n, the parallel ion velocity $v_\parallel$, the electron temperature T_{e} and the ion temperature T_{i}

$$\frac{\partial n}{\partial t} + \frac{\partial}{\partial x}\left(n v_\parallel\right) = S_n, \tag{3}$$

$$\frac{\partial}{\partial t}\left(m_{\mathrm{i}} n v_\parallel\right) + \frac{\partial}{\partial x}\left(m_{\mathrm{i}} n v_\parallel^2 - \eta_{\parallel,\mathrm{i}}\frac{\partial v_\parallel}{\partial x}\right) = -\frac{\partial p_{\mathrm{i}}}{\partial x} + enE + R_{\mathrm{i}} + m_{\mathrm{i}} S_v, \tag{4}$$

$$\frac{\partial}{\partial t}\left(\frac{3}{2}nkT_{\mathrm{e}}\right) + \frac{\partial}{\partial x}\left(\frac{5}{2}v_\parallel nkT_{\mathrm{e}} + q_{\parallel,\mathrm{e}}\right) = -env_\parallel E + v_\parallel R_{\mathrm{e}} + Q_{\mathrm{e}} + S_{E,\mathrm{e}}, \tag{5}$$

$$\frac{\partial}{\partial t}\left(\frac{3}{2}nkT_{\mathrm{i}} + \frac{1}{2}m_{\mathrm{i}} n v_\parallel^2\right) + \frac{\partial}{\partial x}\left(\frac{5}{2}v_\parallel nkT_{\mathrm{i}} + \frac{1}{2}m_{\mathrm{i}} n v_\parallel^3 + q_{\parallel,\mathrm{i}} - v_\parallel \eta_{\parallel,\mathrm{i}}\frac{\partial v_\parallel}{\partial x}\right) = env_\parallel E + v_\parallel R_{\mathrm{i}} + Q_{\mathrm{i}} + S_{E,\mathrm{i}}, \tag{6}$$

complemented by the generalized Ohm's law for electron momentum $enE = -\partial p_{\mathrm{e}}/\partial x + R_{\mathrm{e}}$. S_n, S_v, $S_{E,\mathrm{e}}$ and $S_{E,\mathrm{i}}$ are sources of the density, momentum (here $S_v = 0$) and energy due to cross-field transport. R_{e} and R_{i} ($R_{\mathrm{e}} = -R_{\mathrm{i}}$) are the thermal and friction forces, Q_{e} and Q_{i} ($Q_{\mathrm{e}} = -Q_{\mathrm{i}}$) are the heating due to electron–ion collisions. E is the parallel electric field, p_{i} and p_{e} are the ion and electron static pressures, $\eta_{\parallel,\mathrm{i}}$ is the parallel ion viscosity, m_{i} is the ion mass and $q_{\parallel,\mathrm{e}} = -\kappa_{\parallel,\mathrm{e}}\,\partial(kT_{\mathrm{e}})/\partial x$ and $q_{\parallel,\mathrm{i}} = -\kappa_{\parallel,\mathrm{i}}\,\partial(kT_{\mathrm{i}})/\partial x$ are the parallel thermal heat fluxes.

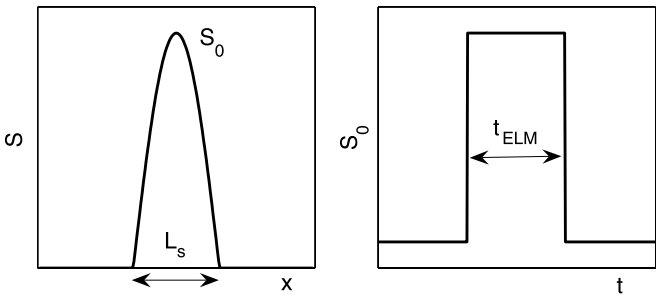

Figure 1. Spatial distribution of the source and its behaviour during the ELM crash.

Recently, the equations were modified to take into account $\nabla_\parallel B$ dependence. The model assumes ambipolar transport of electrons and ions (no net current $j_\parallel = 0$) and the quasi-neutrality condition. The parallel transport coefficients $\eta_{\parallel,\mathrm{i}}$, $\kappa_{\parallel,\mathrm{e}}$ and $\kappa_{\parallel,\mathrm{i}}$ are classical and kinetic corrections are to a certain extent incorporated through flux limiters. Boundary conditions at the targets are the standard sheath boundary conditions $v_\parallel = c_{\mathrm{s}}$, $Q_{\parallel,\mathrm{i}} = \delta_{\mathrm{i}} kT_{\mathrm{i}} n c_{\mathrm{s}}$ and $Q_{\parallel,\mathrm{e}} = \delta_{\mathrm{e}} kT_{\mathrm{e}} n c_{\mathrm{s}}$ with the sound speed c_{s} and using the energy transmission coefficients of the sheath $\delta_{\mathrm{i}} = 3.5$ and $\delta_{\mathrm{e}} = 5.0$. The plasma model is coupled with a fluid model of neutrals, which is not used here. Details are described in [9]. The presented time-dependent runs were performed with the spatial resolution of $N_x = 400$ and the time step approximately $\Delta t \approx 1 \times 10^{-7}$ s. The real time of a typical calculation is in the order of a few seconds.

Even though ELMs are considered to be kinetic phenomena due to very low collisionalities found in the pedestal and it is thought that fluid models cannot adequately describe parallel dynamics associated with ELMs (at the very least without employing kinetic corrections such as heat flux limiters), we aim to compare PIC, Vlasov and fluid results in order to identify limits and gaps of the fluid modelling. The SOLF1D code has already been applied to model transient parallel transport in [1, 9] with attention devoted to SOL plasma fluctuations occurring due to turbulence and the associated effect on plasma parameters at the target.

2.4. Simulation setup

The ELM crash is simulated in one dimension as a transient source of plasma located at the midplane which is represented by the centre of the computational domain (a symmetric case is considered). The parallel extension of the source is characterized by L_{s} in the domain of the size $2L_\parallel$ measured between two targets (figure 1). The source in the parallel direction x is prescribed as a cosine function

$$S_n(x) = S_0^n \cos\left(\frac{\pi x}{L_{\mathrm{s}}}\right) \tag{7}$$

in the interval $\langle -L_{\mathrm{s}}/2, L_{\mathrm{s}}/2\rangle$, which gives an integrated source along the magnetic field $2S_0^n L_{\mathrm{s}}/\pi$. The source is enhanced in time for a period of the ELM crash duration t_{ELM} (rectangular shape in time, different shapes examined in [12] and in the fluid code, see in figure 12, showing only a little effect on the time scale and the maximum target energy flux). The initial

condition is a steady-state solution obtained for a pre-ELM phase, neglecting dynamics of the pre-ELM plasma. The same pre-ELM profile is used for all simulated JET ELMs in the PIC code. The initial profiles can be slightly different in the fluid and Vlasov codes, but it should not substantially influence the results. The background profile is less important compared with the rapid source of plasma due to the ELM crash. Both BIT1 and SOLF1D show almost no sensitivity to the initial profile, unless recycling at the targets is included. This effect is shown later in section 5.

For the purpose of code comparison, only electrons and deuterium ions are included and no plasma–neutral interactions are taken into account. The reference kinetic simulations, we are comparing the fluid model with, were performed without neutrals and impurities. Additionally, benchmark of plasma models separately is more essential, as nowadays fluid codes are usually coupled with Monte Carlo neutral solvers. PIC simulations with neutrals and impurities can be found in [12, 16], showing even better agreement with experiment.

Since the model is only one-dimensional, the particle and energy sources due to cross-field transport from the pedestal into the SOL

$$S_n = \frac{\partial}{\partial r}(n v_\perp), \qquad S_E = \frac{\partial Q_\perp}{\partial r} \tag{8}$$

must be specified. Ideally, we would need to calculate the sources self-consistently with the evolution of the pedestal density and temperature profiles, but this would require more complex modelling tools such as JOREK (a non-linear MHD code) [21]. For benchmarking with PIC simulations in [3], we repeat steps done previously and relate the source to pedestal quantities. Particles of the source are at the pedestal temperature $T_{\rm ped}$ (the same pedestal temperature for electrons and ions is assumed, $T_{\rm e,ped} = T_{\rm i,ped} = T_{\rm ped}$) and the particle source is estimated as

$$S_n \sim n_{\rm ped} c_{\rm s,ped}/L_{\rm s} \tag{9}$$

assuming the upstream density going up to $n_{\rm ped}$ and plasma of the source flowing to the targets with the sound speed found in the pedestal

$$c_{\rm s,ped} = \sqrt{\frac{2kT_{\rm ped}}{m_{\rm i}}}. \tag{10}$$

This corresponds to a simplified balance

$$\boldsymbol{\nabla}\cdot n\boldsymbol{v} \approx 0, \qquad \frac{\partial}{\partial x}(n v_\parallel) \approx S_n \tag{11}$$

at the outboard midplane at the separatrix, assuming that the pedestal density and temperature drops associated with the source are governed by parallel losses on open field lines (see [22]). The particle source S_n is linked to the pedestal density and temperature, which is useful for comparison of resulting target fluxes with experimental scalings (see section 4). The proportionality is expressed by a coefficient A

$$S_0^n \approx A n_{\rm ped} c_{\rm s,ped}/L_{\rm s} \tag{12}$$

which is obtained from the inter-ELM PIC simulation.

Table 1. Summary of parameters used in the model.

Input parameters	$n_{\rm ped}$, $T_{\rm ped}$, $t_{\rm ELM}$, $L_\parallel$, $L_{\rm s}$, R, $L_{\rm pol}$
Derived quantities	S_n, S_E, $\Delta W_{\rm ELM}/\Delta R_{\rm SOL}$, $V_{\rm SOL}/\Delta R_{\rm SOL}$
Output quantities	$Q_\parallel$, $\epsilon_\parallel$, $\Gamma_\parallel$, $N_\parallel$

Second, we assume that the ELM energy is transported across the magnetic field to the SOL due to convection and the total energy source can be written as

$$S_E = \frac{3}{2}k(T_{\rm e,ped} + T_{\rm i,ped})S_n = 3kT_{\rm ped}S_n. \tag{13}$$

We have the same energy source for electrons and ions, although in general different sources and temperatures can be used.

Additionally, we can roughly estimate the total ELM energy as is done in [3]. For convective ELMs, the total input energy can be written as

$$\begin{aligned}\Delta W_{\rm ELM} &\approx 3kT_{\rm ped}\overline{S}V_{\rm SOL}t_{\rm ELM}\\ &\approx 3kT_{\rm ped}\frac{2S_0^n}{\pi}L_{\rm pol}2\pi R\Delta R_{\rm SOL}t_{\rm ELM}.\end{aligned} \tag{14}$$

$\overline{S}$ is the particle source uniform over the poloidal extent $L_{\rm pol}$, i.e. $\overline{S} = 2S_0^n/\pi$, and $V_{\rm SOL}$ is the volume in the SOL where the energy is deposited

$$V_{\rm SOL} = L_{\rm pol}2\pi R\Delta R_{\rm SOL} \tag{15}$$

with the radial extent $\Delta R_{\rm SOL}$. The poloidal length of the source is related to the parallel one as

$$L_{\rm pol} = L_{\rm s}\sin\alpha_{\rm u}. \tag{16}$$

The angle between parallel and poloidal directions $\sin\alpha = B_{\rm pol}/B$ varies along the magnetic field line, therefore $\alpha_{\rm u}$ here expresses an average angle such that equation (16) is satisfied (the index u denotes upstream where the source is located). Because $\Delta W_{\rm ELM}$ can be only estimated using the radial length $\Delta R_{\rm SOL}$, it is convenient to write equation (14) in the following form:

$$\begin{aligned}\frac{\Delta W_{\rm ELM}}{\Delta R_{\rm SOL}} &\approx 3kT_{\rm ped}\frac{2An_{\rm ped}c_{\rm s,ped}}{\pi L_{\rm s}}L_{\rm pol}2\pi Rt_{\rm ELM}\\ &= 6Ap_{\rm ped}c_{\rm s,ped}\sin\alpha_{\rm u}Rt_{\rm ELM}\end{aligned} \tag{17}$$

where the pedestal pressure is defined as $p_{\rm ped} = 2n_{\rm ped}kT_{\rm ped}$.

See table 1 for a summary of the main input parameters and derived quantities in the model. The pedestal density $n_{\rm ped}$, the pedestal temperature $T_{\rm ped}$ and the duration of the transient $t_{\rm ELM}$ are required together with the specification of geometry—the distance of the target from the source centre $L_\parallel$ and the parallel length of the source $L_{\rm s}$. The main output of the code is quantities at the target such as the energy flux $Q_\parallel$ and $\epsilon_\parallel \equiv \int Q_\parallel\,{\rm d}t$ and the particle flux $\Gamma_\parallel$ and $N_\parallel \equiv \int \Gamma_\parallel\,{\rm d}t$. These quantities can be projected onto the poloidal plane as $Q_{\rm pol} = Q_\parallel\sin\alpha_{\rm t}$, etc, using the local angle $\alpha_{\rm t}$.

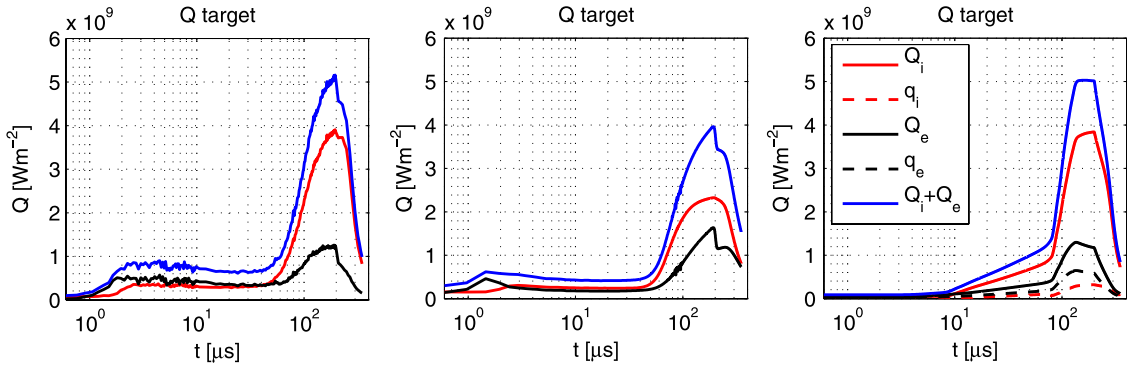

Figure 2. Parallel target energy flux for the reference case calculated by (left) the PIC code, (middle) the Vlasov code and (right) the fluid code. In the fluid model, the parallel ion viscosity is limited and the total energy source due to the ELM is prescribed to be shared by ions and electrons as 3 : 1, see the discussion below.

3. Results and comparison

3.1. Reference simulation

An ELM crash described by a set of pedestal parameters typical for JET type I ELMs is taken as a reference case (see [12], JET shot number 62221):

$$n_{\mathrm{ped}} = 5 \times 10^{19}\ \mathrm{m}^{-3}, \quad T_{\mathrm{ped}} = 1.5\ \mathrm{keV}, \quad t_{\mathrm{ELM}} = 200\ \mu\mathrm{s}.$$

Geometric parameters are

$$L_{\parallel} \approx 40\ \mathrm{m}, \qquad L_{\mathrm{s}} \approx 25\ \mathrm{m}.$$

From (14), we can obtain corresponding ELM power $\Delta W_{\mathrm{ELM}} \approx 0.4\,\mathrm{MJ}$ using the same values as in [3]: $\Delta R_{\mathrm{SOL}} = 10\,\mathrm{cm}$, $R = 3\,\mathrm{m}$ and $L_{\mathrm{pol}} = 2.6\,\mathrm{m}$ ($L_{\mathrm{pol}} = L_{\mathrm{s}} \sin\alpha_{\mathrm{u}}$ with $\alpha_{\mathrm{u}} = 6^{\circ}$), but note that ΔR_{SOL} is just a scaling parameter for ΔW_{ELM}. In PIC simulations, the angle α is fixed ($\alpha_{\mathrm{u}} = \alpha_{\mathrm{t}} = 6^{\circ}$), while in this paper, we generally distinguish between target and upstream angles.

Figure 2 shows the main analysed quantity, the total parallel energy flux at the target $Q_{\parallel}$, electron and ion components $Q_{\parallel,\mathrm{e}}$ and $Q_{\parallel,\mathrm{i}}$ and in the case of the fluid code also thermal fractions $q_{\parallel,\mathrm{e}}$ and $q_{\parallel,\mathrm{i}}$ due to heat conduction. Note that $Q_{\parallel}$ is the energy flux deposited on the target in the direction of the magnetic field, not the power load which is referred to the flux perpendicular to the surface.

The ELM energy is transported along the magnetic field preferentially by convection in all cases (low-collisionality case, no plasma–neutral interactions present). In the fluid model (figure 2 right and more details in the appendix), we observe two main time scales of the parallel transport corresponding to conduction (the structure appearing between $t \approx 10$–$80\,\mu\mathrm{s}$) and convection (the main maximum, the time scale can be estimated as $\tau_{\parallel} \approx L_{\parallel}/c_{\mathrm{s,ped}} \approx 104\,\mu\mathrm{s}$). The first structure does not appear so strongly in the PIC model and could probably be modified or eliminated using heat flux limiters. On the other hand, we do not see any response at the target before $10\,\mu\mathrm{s}$ in comparison with the rise of the energy flux at the target in the PIC and Vlasov simulations in figure 2 (left and middle), which appears due to fast ELM particles and a reaction of the background plasma (the time scale is $\tau_{\parallel}^{\mathrm{e}} \approx L_{\parallel}/v_{\mathrm{th,ped}}^{\mathrm{e}} \approx 2.4\,\mu\mathrm{s}$, $v_{\mathrm{th,ped}}^{\mathrm{e}}$ is the electron thermal speed in the pedestal). Such fast response is not observed in kinetic simulations if the transient propagates in the vacuum. These two features, clearly visible in log scale, define the main differences in fluid and kinetic results.

The Vlasov and PIC simulations are in fair agreement as far as the total energy flux is concerned, though the peak value is slightly underestimated by the Vlasov model. In both cases, the input energies are equally shared between ions and electrons (unlike the fluid code where the energy source is redistributed as $S_{E,\mathrm{i}}/S_{E,\mathrm{e}} = 3$, see section 3.3). In general, the Vlasov code displays a lower energy flux for ions but a higher one for electrons compared with PIC. It must be noted that the Vlasov code is completely collisionless, whereas collisions are included in the PIC simulation. The effect of collisions may thus be to enhance the energy transfer from the electron to the ion population. A simulation where collisions are removed from the PIC code indeed produces results very similar to those obtained with the Vlasov code, for both the ion and electron energy fluxes [23].

It is worth mentioning that the power to the target can also be described well by a free-streaming model [24] (no collisions, no background plasma). Earlier, it was demonstrated that the heat pulse shape at the target calculated analytically agrees with the shape typically observed in experiment [25]. Results from the free-streaming model (with an *ad hoc* assumption that electrons transfer all of their parallel energy to the ions so that both species are quickly accelerated to the sound speed) show good agreement with both the Vlasov and PIC codes. These comparisons will be published in [26]. To properly compare the free-streaming model with the kinetic codes, the analytic impulse response must be numerically convolved with the temporally and spatially distributed sources that were used in the kinetic codes. However, in the case when the source is localized in space at the distance $L_{\parallel}$ from the target and distributed in time as a step function with duration t_{ELM}, an analytic solution for the parallel energy flux to one target can be found as follows:

$$\frac{Q_{\parallel}}{\epsilon_{\mathrm{inp}}} = \frac{1}{3}\frac{\tau_{\parallel}}{t_{\mathrm{ELM}}\sqrt{2\pi}}\frac{1}{t}\exp\left(-\frac{1}{2}\left(\frac{\tau_{\parallel}}{t}\right)^2\right) + \frac{1}{2t_{\mathrm{ELM}}}\left(1 - \mathrm{erf}\left(\frac{\tau_{\parallel}}{\sqrt{2}t}\right)\right), \quad \text{if} \quad 0 < t \leqslant t_{\mathrm{ELM}},$$

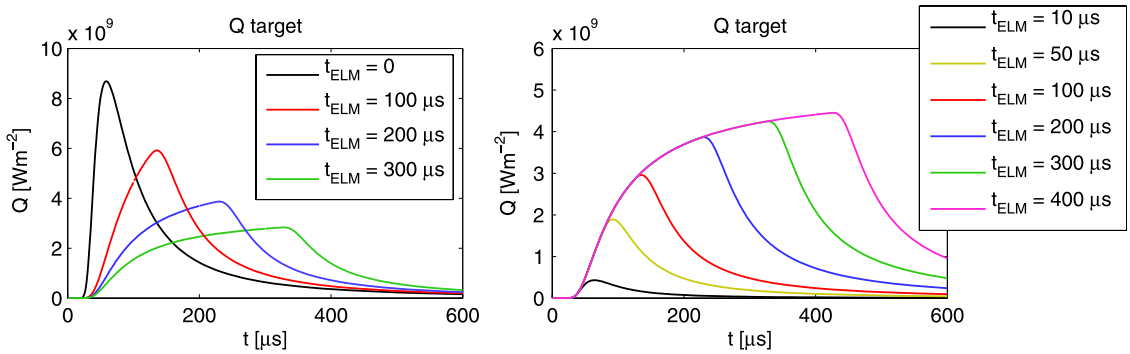

Figure 3. Parallel target energy flux calculated by the free-streaming model for different pulse durations with (left) fixed total input energy $\epsilon_{\rm inp} \approx 2\,{\rm MJ\,m^{-2}}$ (the same as in the reference case with $t_{\rm ELM} = 200\,\mu$s in figure 2), (right) input energy $\epsilon_{\rm inp} = t_{\rm ELM} \int S_E\,{\rm d}x$ and constant energy source S_E. $\tau_\parallel \approx 104\,\mu$s in all cases.

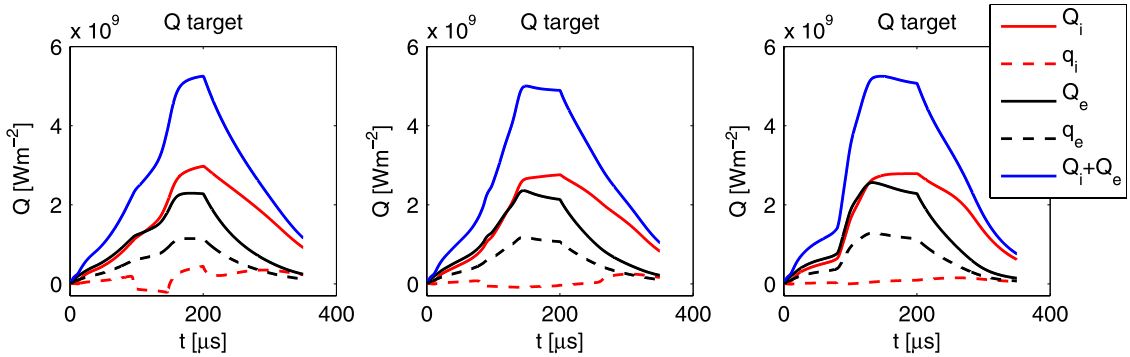

Figure 4. Parallel target energy flux modelled by the fluid code for three different ion viscosity limiters: $\beta = 4/7$ on the left (weaker limiting), $\beta = 0.3$ in the middle and $\beta = 0.1$ on the right (stronger limiting). In this case, the electron and ion energy sources are equal, $S_{E,\rm i}/S_{E,\rm e} = 1$.

$$\frac{Q_\parallel}{\epsilon_{\rm inp}} = \frac{1}{3}\frac{\tau_\parallel}{t_{\rm ELM}\sqrt{2\pi}}\left(\frac{1}{t}\exp\left(-\frac{1}{2}\left(\frac{\tau_\parallel}{t}\right)^2\right) - \frac{1}{t - t_{\rm ELM}} \times \exp\left(-\frac{1}{2}\left(\frac{\tau_\parallel}{t - t_{\rm ELM}}\right)^2\right)\right) + \frac{1}{2t_{\rm ELM}} \times \left({\rm erf}\left(\frac{\tau_\parallel}{\sqrt{2}(t - t_{\rm ELM})}\right) - {\rm erf}\left(\frac{\tau_\parallel}{\sqrt{2}t}\right)\right), \quad \text{if} \quad t > t_{\rm ELM}. \tag{18}$$

The energy flux $Q_\parallel$ is normalized to the total input energy during the transient $\epsilon_{\rm inp} = t_{\rm ELM} \int S_E {\rm d}x$. Figure 3 shows solutions for different pulse durations $t_{\rm ELM}$.

3.2. Kinetic correction to parallel ion viscosity

During the ELM crash, it was necessary to apply an ion viscous flux limit in the fluid code, because the results with the classical value of ion viscosity looked unphysical (viscous part of the ion energy flux at the target exceeding the total energy flux controlled by the boundary condition by two orders of magnitude). We use the limiter $\beta = 0.1$ in the reference case. A kinetic simulation in [17] shows a decrease of the poloidally averaged limiter during the early phase of the ELM crash from $\beta = 0.5$ down to $\beta = 0.1$ and then a slow relaxation back to the pre-ELM value. The influence of the viscosity limiter on the time characteristics and the rise phase of the parallel target energy flux is shown in figure 4, the right panel is for $\beta = 0.1$ as in the reference case. The energy transfer is first dominated by diffusive processes (before 80 μs) and later by convection accompanied by viscous friction. The convection time scale is modified by viscous effects and the maximum energy flux at the target is observed later when the viscosity is higher (figure 4 left); however, the energy flux amplitude is almost the same in all cases. No heat flux limiters are employed and parallel heat flux conductivities are of Spitzer–Härm form.

3.3. Electron versus ion power fractions

Another difference between the kinetic and fluid descriptions is the ratio between electron and ion energy fluxes at the target. The PIC simulation shows that the ELM energy is carried to the targets mainly by the ion component (figure 2 left) for the same initial energy source to electrons and ions, while in the fluid model, the energy transport is shared more or less equally by electrons and ions. Therefore, in SOLF1D, we prescribed that the input energy goes to ion and electron channels as 3 : 1, i.e. the ratio of the energy sources is $S_{E,\rm i}/S_{E,\rm e} = 3$ (see figure 5 for comparison). Nevertheless, this artificial modification of power fractions does not have any substantial effect on the total energy flux observed at the target and the amplitude remains unchanged.

An explanation for the observed discrepancy lies in the way the sheath is treated in the models. Kinetic modelling follows the formation of the sheath and the establishment of the sheath potential during the ELM crash, while in the fluid model, the sheath is not resolved. It is represented by a boundary condition described by fixed sheath energy

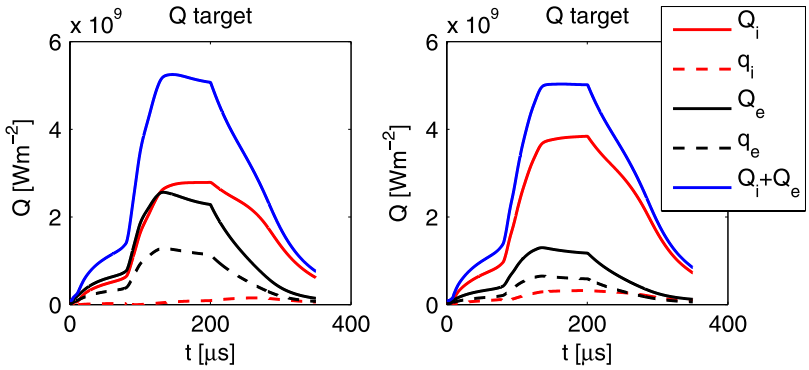

Figure 5. Parallel target energy flux modelled by the fluid code for input power fractions to ions and electrons 1 : 1 (left) and 3:1 (right).

transmission coefficients which in reality evolve during the energetic transient. The sheath potential drop in the kinetic codes is modified due to faster ELM electrons in a way the electron power to the divertor is reduced and the exact resolution of the sheath is required to model this effect. The reader is referred to [17] for more details about kinetic studies of the sheath during an ELM crash.

3.4. ELM crash duration

Figures 6–8 show the evolution of target energy fluxes with various ELM crash durations as simulated by PIC, Vlasov and fluid models. Recall that by changing t_{ELM} for the same pedestal density and temperature, we also change the total ELM energy ΔW_{ELM}, see equation (14). In first 50 μs, only plasma background contributes to the energy flux observed at the target. In the PIC and Vlasov codes (figures 6–7), it is the thermal background plasma that is pushed towards the divertor in response to the ELM pulse. There is also an early burst of fast ELM electrons which escape the attraction of ions; however, their contribution is typically two orders of magnitude smaller [18]. In the fluid code, it is the heat diffusion that propagates on the plasma background. After 50 μs, the energy flux rises due to convection. If the transient duration t_{ELM} is long compared with $\tau_{\parallel}$ (figures 6–8 (right)), a plateau in the profile of the target energy flux appears. The temperature of plasma in front of the target increases to a certain maximum (given by the temperature of hot ELM particles) and the energy flux saturates, while there is almost no temperature gradient along the field line.

In the fluid code, the first structure between 10 and 80 μs is more pronounced when the transient is short (left panel in figure 8) as the main peak energy flux is smaller. The fraction of power deposited at the target by heat conduction is important in the total balance, in contrast to the cases with the duration of 200 or 400 μs. For even shorter transients, this fraction becomes dominant and discrepancies between fluid and kinetic results are expected.

4. Parametrization of simulation results

4.1. Energy fluence ϵ

A series of fluid and Vlasov runs were performed for various pedestal parameters corresponding to PIC simulations of parallel transport during JET ELMs referred to in [3]. From results, we can obtain an expression for the energy flux at the target integrated over time, $\epsilon_{\parallel} \equiv \int_{\mathrm{ELM}} Q_{\parallel}\,\mathrm{d}t$ (the energy fluence), in terms of the pedestal density, temperature and ELM crash duration

$$\epsilon_{\parallel} \approx 0.56 p_{\mathrm{ped}} c_{\mathrm{s,ped}} t_{\mathrm{ELM}} \tag{19}$$

where $p_{\mathrm{ped}} = 2n_{\mathrm{ped}} k T_{\mathrm{ped}}$ is the pedestal pressure and $c_{\mathrm{s,ped}} = \sqrt{2kT_{\mathrm{ped}}/m_{\mathrm{i}}}$ is the pedestal sound speed. The fit can be derived analytically, without using the simulation results, based on the assumptions in section 2.4. Expression (19) results from the energy conservation in the one-dimensional model where the targets are the only loss channel, i.e. all input SOL energy due to the ELM leaves the system at the targets, $\epsilon_{\parallel} = \frac{1}{2} t_{\mathrm{ELM}} \int S_E\,\mathrm{d}x$. We use $S_E = 3kT_{\mathrm{ped}} S_n$, see equation (13), and approximate the particle source by $S_0^n \approx A n_{\mathrm{ped}} c_{\mathrm{s,ped}}/L_{\mathrm{s}}$, see equation (12). The source scales with a constant $A \approx 1.2$ which is calculated from the inter-ELM PIC simulation. It is reflected in the coefficient 0.56 appearing in equation (19), which corresponds to $3A/2\pi$. Analogously, we could obtain

$$N_{\parallel} \approx 0.38 n_{\mathrm{ped}} c_{\mathrm{s,ped}} t_{\mathrm{ELM}} \tag{20}$$

where $N_{\parallel} \equiv \int_{\mathrm{ELM}} \Gamma_{\parallel}\,\mathrm{d}t$ is the time-integrated particle flux at the target (the particle fluence) and the coefficient 0.38 corresponds to A/π.

Figure 9 shows our fit for several combinations of the pedestal density and temperature defined in tables 2–4 according to simulations documented in [3]. On the left, we can see $\epsilon_{\parallel}$ versus $p_{\mathrm{ped}} c_{\mathrm{s,ped}} t_{\mathrm{ELM}}$ resulting from the PIC, fluid and Vlasov models and the linear dependence given by equation (19). A good match of all codes in figure 9 on the left is not surprising, $\epsilon_{\parallel}$ calculated in the codes should agree with equation (19), which just reflects the energy conservation in the codes along the field line. On the right, $\epsilon_{\parallel}$ is plotted as a function of p_{ped} only, showing a spread for runs with different t_{ELM}. The interval of time integration is t_{ELM} + 150 μs in all cases.

For the simulated JET ELMs, we approximate ΔW_{ELM} as a function of the particle source using a radial length ΔR_{SOL} in the SOL where the ELM power is deposited, see equation (14) and (12). We can then write $\epsilon_{\parallel}$ from the expression (19) (the prefactor 0.56 is equivalent to $3A/2\pi$) in the following way:

$$\epsilon_{\parallel} \approx \frac{1}{2} \frac{\Delta W_{\mathrm{ELM}}}{2\pi R \Delta R_{\mathrm{SOL}} \sin\alpha_{\mathrm{u}}}. \tag{21}$$

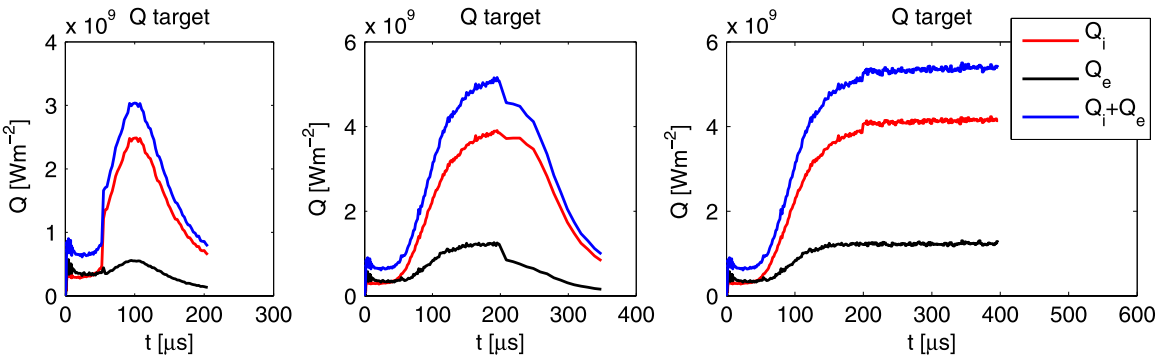

Figure 6. Parallel target energy flux calculated by the PIC code for the ELM crash duration 53 μs (left), 200 μs (middle) and 400 μs (right).

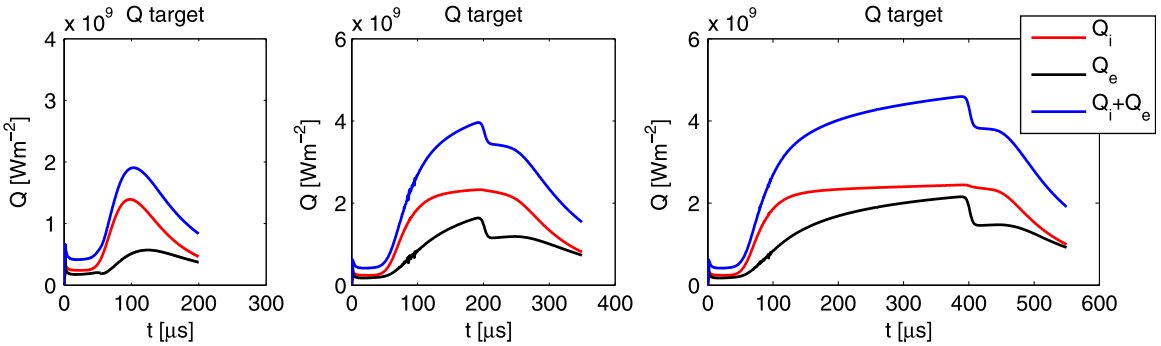

Figure 7. Parallel target energy flux calculated by the Vlasov code for the ELM crash duration 53 μs (left), 200 μs (middle) and 400 μs (right).

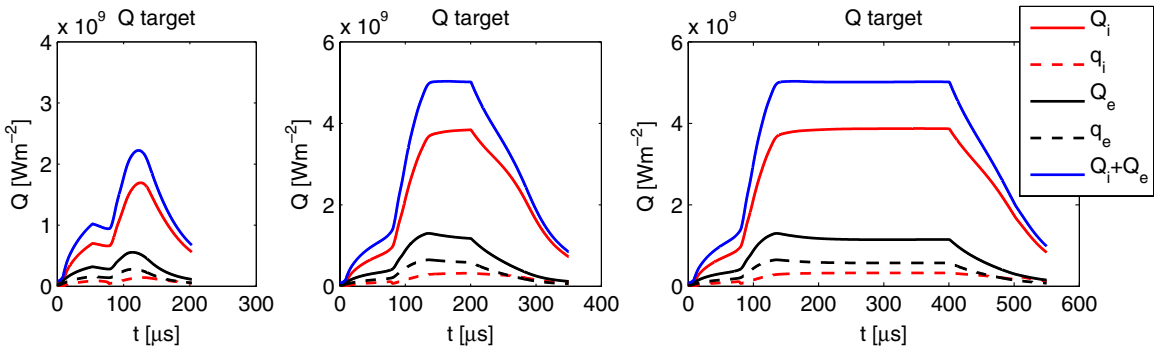

Figure 8. Parallel target energy flux calculated by the fluid code for the ELM crash duration 53 μs (left), 200 μs (middle) and 400 μs (right).

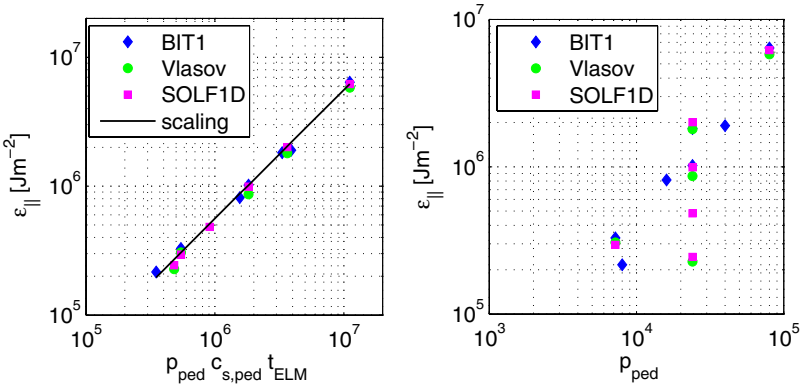

Figure 9. $\epsilon_\parallel$ versus $p_{\rm ped}c_{\rm s,ped}t_{\rm ELM}$ (left) and $\epsilon_\parallel$ versus $p_{\rm ped}$ (right).

Table 2. Summary of PIC simulations. Note that not all simulations from [3] were included, since some of them were too short to calculate values of $\epsilon_\parallel$ at the target.

$n_{\rm ped}$ (10^{19} m^{-3})	5.0	1.5	2.0	5.0	1.5	5.0	5.0
$T_{\rm ped}$ (keV)	0.5	1.5	2.5	1.5	5.0	2.5	5.0
$\Delta W_{\rm ELM}$ (MJ)	0.078	0.122	0.345	0.400	0.750	0.795	2.460
$t_{\rm ELM}$ (μs)	200	200	200	200	200	200	200
$Q_\parallel^{\rm max}$ (GW m^{-2})	1.01	1.46	4.10	5.16	9.20	9.83	31.14
$\epsilon_\parallel$ (MJ m^{-2})	0.22	0.33	0.81	1.02	1.82	1.90	6.41

Table 3. Summary of Vlasov simulations.

$n_{\rm ped}$ (10^{19} m^{-3})	1.5	5.0	5.0	5.0	5.0
$T_{\rm ped}$ (keV)	1.5	1.5	5.0	1.5	1.5
$\Delta W_{\rm ELM}$ (MJ)	0.122	0.400	2.460	0.110	0.810
$t_{\rm ELM}$ (μs)	200	200	200	53	400
$Q_\parallel^{\rm max}$ (GW m^{-2})	1.37	3.96	27.12	1.91	4.59
$\epsilon_\parallel$ (MJ m^{-2})	0.31	0.87	5.81	0.23	1.80

Table 4. Summary of fluid runs.

$n_{\rm ped}$ (10^{19} m^{-3})	1.5	5.0	5.0	5.0	5.0	5.0
$T_{\rm ped}$ (keV)	1.5	1.5	5.0	1.5	1.5	1.5
$\Delta W_{\rm ELM}$ (MJ)	0.122	0.400	2.460	0.110	0.200	0.810
$t_{\rm ELM}$ (μs)	200	200	200	53	100	400
$Q_\parallel^{\rm max}$ (GW m^{-2})	1.57	5.03	31.23	2.22	3.91	5.03
$\epsilon_\parallel$ (MJ m^{-2})	0.30	0.99	6.20	0.24	0.48	2.01

In the poloidal direction ($\epsilon_{\rm pol} = \epsilon_\parallel \sin\alpha_{\rm t}$)

$$\epsilon_{\rm pol} \approx \frac{1}{2}\frac{\Delta W_{\rm ELM}}{A_{\rm w}}. \qquad (22)$$

$\Delta R_{\rm SOL}$ is directly related to the wetted area $A_{\rm w} = 2\pi R \Delta R_{\rm SOL} FX$ and the factor $FX = \sin\alpha_{\rm u}/\sin\alpha_{\rm t}$ measures the flux expansion. The wetted area is defined as $A_{\rm w} \equiv E_{\rm ELM}/\epsilon^{\rm max}$, $E_{\rm ELM} \equiv 2\pi R \int \epsilon \, {\rm d}r$. If we assume an exponential profile along the target $\epsilon(r) \sim \exp(-r/\lambda)$, where r is the radial coordinate perpendicular to the poloidal direction (mapped to the outer midplane), $\Delta R_{\rm SOL}$ is equivalent to λ.

4.2. Peak energy flux $Q^{\rm max}$

An expression for the peak parallel energy flux at the target in terms of the pedestal quantities is constructed, based on simulations in figures 6–8 and runs specified in tables 2–4. We can notice that a longer transient with the duration 400 μs (meaning also larger ELM power $\Delta W_{\rm ELM}$) gives the same peak energy flux compared with 200 μs ELM crash (both with the same pedestal density and temperature). To capture ELMs with various time durations into one fit, it is therefore reasonable to assume two branches, the first one is the rise phase of the energy flux and the second one is the plateau (representing the maximum energy flux for given pedestal parameters). The moment the maximum is reached is roughly defined by the time scale of parallel particle advection $\tau_\parallel \approx L_\parallel/c_{\rm s,ped}$. We get an approximate expression based on code results

$$Q_\parallel^{\rm max} \approx 0.55 p_{\rm ped} c_{\rm s,ped} \min\left\{1, \frac{t_{\rm ELM}}{\tau_\parallel}\right\}, \qquad (23)$$

but practically, for the majority of investigated JET ELMs for which 200 μs is assumed, the expression reduces to $Q_\parallel^{\rm max} \sim p_{\rm ped} c_{\rm s,ped}$ dependence and $Q_\parallel^{\rm max} \approx \epsilon_\parallel/t_{\rm ELM}$. The heat pulse shape and the peak value $Q_\parallel^{\rm max}$ are slightly sensitive to the parallel size of the source $L_{\rm s}$, see below, while there is no effect of $L_{\rm s}/L_\parallel$ on the energy fluence $\epsilon_\parallel$.

Figure 10 shows again our fit for a series of simulations from tables 2–4. On the left, we can see $Q_\parallel^{\rm max}$ from the codes and $Q_\parallel^{\rm max}$ calculated from equation (23) as a function of $p_{\rm ped} c_{\rm s,ped} \min\{1, t_{\rm ELM}/\tau_\parallel\}$. On the right, the same quantity is plotted versus $p_{\rm ped} c_{\rm s,ped}$ only, showing a strong departure from the linear fit only for the shortest transient of 53 μs.

Similarly to equation (21), we can obtain an alternative relation for $Q_\parallel^{\rm max}$ displaying the energy balance in the SOL, if we express it as a function of $\Delta W_{\rm ELM}$

$$Q_\parallel^{\rm max} \approx 0.49 \frac{\Delta W_{\rm ELM}}{2\pi R \Delta R_{\rm SOL} \sin\alpha_{\rm u} t_{\rm ELM}} \min\left\{1, \frac{t_{\rm ELM}}{\tau_\parallel}\right\}. \qquad (24)$$

The obtained fits (19) and (23) deserve several comments:

- Since the relation between the pedestal pressure drops, the associated energy released into the SOL and the energy source in the SOL due to the transient cannot be self-consistently modelled here, the source is approximated by equation (12), see section 2.4. This approximation could be compared with a two-dimensional code [2] or an MHD code such as JOREK. The relevance of the assumptions (12) and (13) is important for the derived fits, even though the PIC code shows good agreement with experiment in many cases.
- For a direct comparison with experiment, the parallel energy flux must be recalculated as the flux to the divertor plate. For example, for the JET shot 74312, the pitch angles are $\sin\alpha_{\rm u} \approx 0.25$ and $\sin\alpha_{\rm t} \approx 0.08$ and the inclination angle of the target with respect to the field

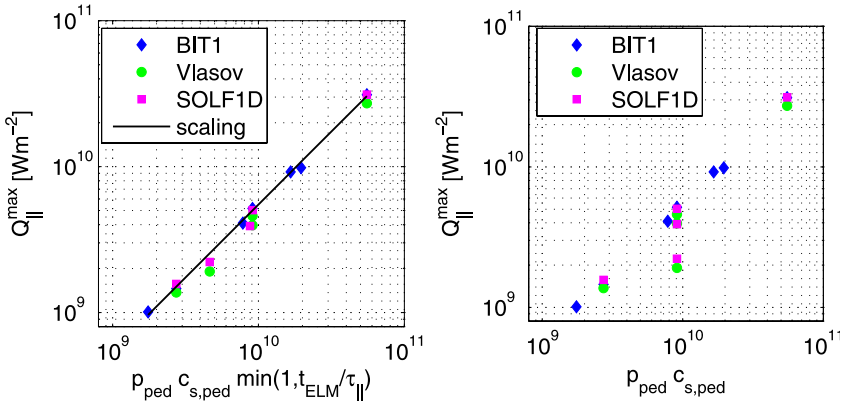

Figure 10. $Q_{\parallel}^{max}$ versus $p_{ped}c_{s,ped}\min\{1, t_{ELM}/\tau_{\parallel}\}$ (left) and $Q_{\parallel}^{max}$ versus $p_{ped}c_{s,ped}$ (right).

line in the poloidal cross section is 33°. This would give a field line angle at the target plate approximately 2.5°. In [3, 12], larger $\alpha_t = 6°$ is assumed and the poloidal flux, $Q_{pol} = Q_{\parallel} \sin\alpha_t$, would be a factor of ≈10 smaller than the parallel flux. In addition, a radially non-uniform profile of power loads is taken into account, since Q_{pol} or $Q_{\parallel}$ are calculated at the position just behind separatrix. In [12], an exponential profile $Q(r) \sim \exp(-r/\lambda)$ is assumed reducing the target energy flux with a factor of 0.637 to the average value over the interval $\langle 0, \lambda\rangle$ comparable to experimental data.

- Further, it is expected that the peak energy flux at the target would be reduced in the presence of collisions with neutrals and radiation cooling (see discussion in section 5). The coefficient 0.55 in equation (23) represents in this sense a certain maximum.

4.3. Predictions for ITER

The fits obtained for $\epsilon_{\parallel}$ and $Q_{\parallel}^{max}$ for JET ELMs are used for conditions expected on ITER. We take

$$n_{ped} = 6 \times 10^{19}\ \mathrm{m}^{-3}, \quad T_{ped} = 5\ \mathrm{keV},$$
$$t_{ELM} = 200\ \mu\mathrm{s}, \quad L_{\parallel} = 115\ \mathrm{m}$$

as representative ITER values, similarly as in [12], but in deuterium plasma only. This gives $p_{ped} \approx 96$ kPa, $c_{s,ped} \approx 7 \times 10^5$ ms^{-1} and $\tau_{\parallel} \approx 166\,\mu$s. The scalings (19) and (23) lead to

$$\epsilon_{\parallel} \approx 7.44\ \mathrm{MJ\,m^{-2}}, \qquad Q_{\parallel}^{max} \approx 36.52\ \mathrm{GW\,m^{-2}}.$$

The energy fluence and flux in the fitting expressions are expressed as vectors parallel to the magnetic field and can be recalculated to fluxes perpendicular to the target using local angles of the magnetic field and target inclination. If we use the same $\alpha_t = 4°$ as in [12] (for further comparison with results in [12]), the fluence and flux projected onto the poloidal plane ($Q_{pol}^{max} = Q_{\parallel}^{max} \sin\alpha_t$, $\epsilon_{pol} = \int_{ELM} Q_{pol}\, dt$) are

$$\epsilon_{pol} \approx 0.52\ \mathrm{MJ\,m^{-2}}, \qquad Q_{pol}^{max} \approx 2.55\ \mathrm{GW\,m^{-2}},$$

just around the limit of 0.5 MJ m^{-2} mentioned in [4]. For field line angle at the target $\alpha \approx 2.5°$ reported elsewhere [27], perpendicular fluence and flux would be

$$\epsilon_{\perp} \approx 0.32\ \mathrm{MJ\,m^{-2}}, \qquad Q_{\perp}^{max} \approx 1.59\ \mathrm{GW\,m^{-2}}.$$

The link between $\epsilon_{\parallel}$ and the pedestal parameters is imposed by assuming convective ELMs (13) and a simplified balance between losses from the pedestal (the radial ELM source) and parallel losses in the SOL with the upstream density going up to the pedestal value and the hot ELM plasma streaming towards targets with the pedestal sound speed (12). The corresponding ELM energy can be estimated from equation (17) if we assume a certain radial size of the filament in the SOL ΔR_{SOL}. Using $R = 6$ m, $L_s = 75$ m and $L_{pol} = 5.2$ m, we get $\Delta W_{ELM} \approx 4$ MJ for $\Delta R_{SOL} = 10$ cm or $\Delta W_{ELM} \approx 1$ MJ for $\Delta R_{SOL} = 2.5$ cm. Recall that for convective ELMs, the simple balance between parallel and perpendicular transport assumed here results in ΔR_{SOL} proportional to the radial width of the ELM affected area ΔR_{ped}, see the appendix.

A PIC simulation reported earlier in [12] gives $Q_{pol}^{max} \approx 1.6$ GW m^{-2}, somewhat lower than the obtained value from the fit $Q_{pol}^{max} \approx 2.55$ GW m^{-2}. For the purpose of a direct comparison with PIC results, an additional extrapolation is performed by the fluid code (neglecting neutrals and impurities). A transient of 200 μs is modelled in the one-dimensional geometry described by $L_{\parallel} = 115$ m and $L_s = 75$ m (this means the same poloidal angle where the power from the pedestal is expelled into the SOL as in the previous JET case and the same $L_s/L_{\parallel}$ ratio). $L_{\parallel}$ is taken from [12] and corresponds to a flux tube just outside the separatrix. The particle and energy sources into the SOL are calculated as described in section 2.4. Pre-ELM upstream density and temperatures are $n \approx 3 \times 10^{19}$ m^{-3}, $T_e \approx 160$ eV and $T_i \approx 260$ eV (similar to those in [12] which were obtained from a SOLPS solution). As a result of the fluid code, we obtain the energy fluence during the ELM crash $\epsilon_{\parallel} \approx 7.15$ MJ m^{-2} (integrating $Q_{\parallel}$ over t_{ELM}+300 μs) and the peak energy flux $Q_{\parallel}^{max} \approx 31.11$ GW m^{-2}, confirming the values from fitting expressions using n_{ped} and T_{ped} directly. Corresponding fluence and flux in the poloidal direction is $\epsilon_{pol} \approx 0.5$ MJ m^{-2} and $Q_{pol}^{max} \approx 2.17$ GW m^{-2}, using $\alpha_t = 4°$. The angle α is again

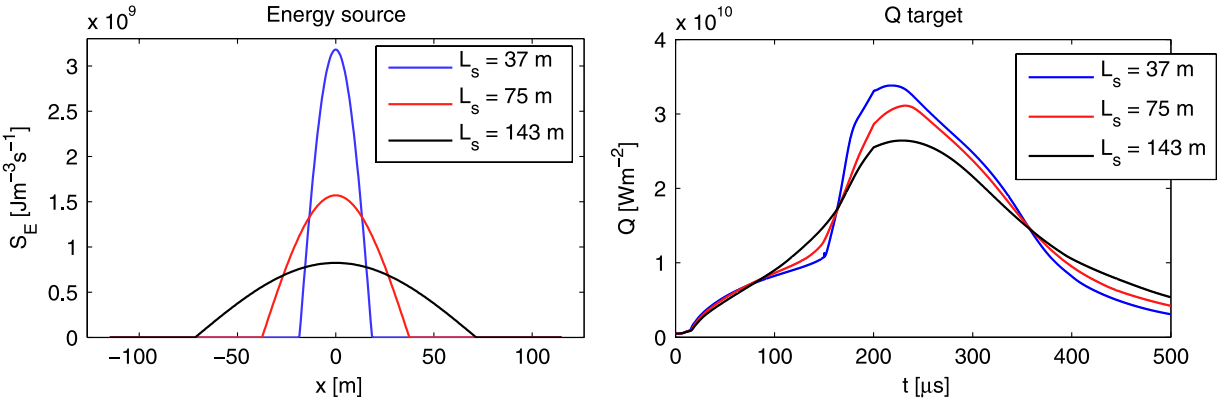

Figure 11. Impact of the parallel size of the source on the peak energy flux at the target. Three runs of the fluid code with different distribution of the particle and energy sources along the field line (left) and corresponding parallel target energy flux (right). Compare with a PIC simulation in [12].

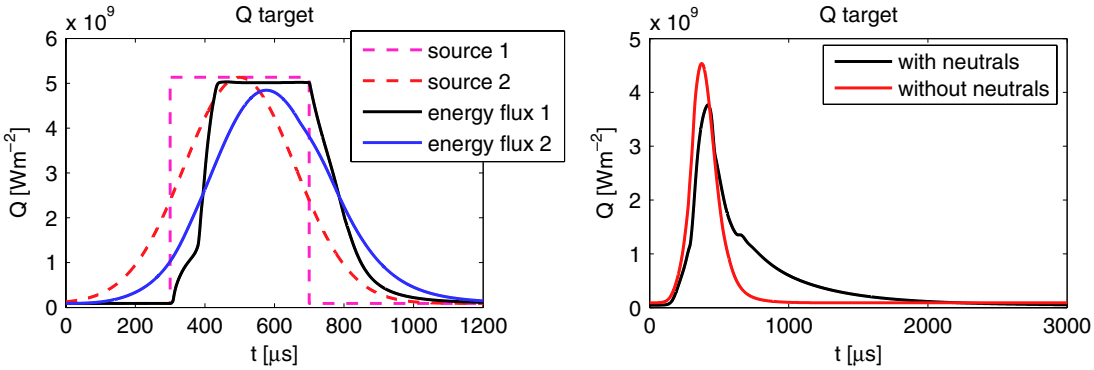

Figure 12. Effect of the temporal distribution of the source on the energy flux at the target (left)—rectangular versus Gaussian shape with $t_{\mathrm{ELM}} = 400\,\mu$s. Effect of neutrals on the time scale (right)—$t_{\mathrm{ELM}} = 200\,\mu$s and the source is Gaussian in time. Pre-ELM profiles are different at the target (no recycling versus low recycling), but they match at the midplane.

fixed in PIC simulations along the field line (i.e. $\alpha_{\mathrm{t}} = \alpha_{\mathrm{u}}$) and α_{u} has been calculated for ITER in [12] from an equilibrium used by SOLPS as an average angle so that the total lengths of the simulated flux tube in the parallel ($L_{\parallel}^{\mathrm{tot}} = 2L_{\parallel}$) and poloidal ($L_{\mathrm{pol}}^{\mathrm{tot}}$) directions and satisfy $L_{\mathrm{pol}}^{\mathrm{tot}} = L_{\parallel}^{\mathrm{tot}} \sin\alpha_{\mathrm{u}}$.

One of the reasons the PIC simulation predicts lower $Q_{\mathrm{pol}}^{\mathrm{max}}$ is the presence of tritium (50%) leading to 10% decrease in the pedestal sound speed compared with deuterium plasma. The second reason is a different profile of the source in the parallel direction assumed in the fluid and PIC codes. The expressions (19) and (23) were obtained with constant ratio $L_{\mathrm{s}}/L_{\parallel} \approx 0.62$ and the same ratio is used in the fluid run for ITER. While the total input energy is the same in both codes, the PIC model in [12] assumes twice broader source $L_{\mathrm{s}} \approx 143$ m with lower amplitude. Figure 11 shows the impact of the source broadening on the energy flux observed at the target. A source with $L_{\mathrm{s}} = 143$ m leads to 15% decrease of $Q_{\parallel}^{\mathrm{max}}$ and $Q_{\mathrm{pol}}^{\mathrm{max}}$ compared with the one with $L_{\mathrm{s}} = 75$ m assumed above. If we combine the effect of tritium and the source extension, we get a perfect quantitative match of $Q_{\mathrm{pol}}^{\mathrm{max}}$ in the fluid and PIC codes. In the studied range of $L_{\mathrm{s}}/L_{\parallel} \approx 0.32$–$1.24$, there is an inverse dependence of $Q_{\parallel}^{\mathrm{max}}$ on L_{s} and the energy flux scales approximately as $Q_{\parallel}^{\mathrm{max}}/Q_0 \approx 0.9(L_{\mathrm{s}}/L_{\parallel})^{-0.2}$ where $Q_0 = Q_{\parallel}^{\mathrm{max}}(L_{\mathrm{s}}/L_{\parallel} \approx 0.65)$. A similar test for JET ELM from section 3.1 shows a similar trend, but with different powers, $Q_{\parallel}^{\mathrm{max}}/Q_0 \approx (L_{\mathrm{s}}/L_{\parallel})^{-0.06}$, and the change of $Q_{\parallel}^{\mathrm{max}}$ is not large, approximately 4% decrease for twice broader source and 4% increase for twice sharper source.

5. Conductive ELMs and additional questions

There are several effects coming into question, which are not investigated here. In the previous sections, we assume purely convective ELMs. This seems to be a reasonable assumption for pedestal collisionalities at JET around $\nu_{\mathrm{e}}^{*} \approx 0.5$ and larger (see [28], also for ν_{e}^{*} definition), while for lower collisionalities, a large part of energy can be carried by heat conduction (which could be the case for ITER). Secondly, we could speculate about the effect of neutral recycling close to the targets, which is not taken into account. H-mode is often associated with low-collisional SOL plasma and the presence of neutrals is thought not to influence the studied phenomena dramatically, which was examined earlier by the PIC code [12, 16] (a simulation shows 30% decrease of $Q_{\parallel}^{\mathrm{max}}$ and agreement with experiment improves when impurity radiation and recycling are involved, and a small impact on the time scale is observed). It would be worth looking at the effect of collisions in operational conditions where ELMs occur with high-recycling or detachment at the targets, a regime envisaged for ITER. Figure 12 (results of the fluid code) is studying the influence of time distribution of the source (left) and the effect of neutrals (right) on the time scales observed at

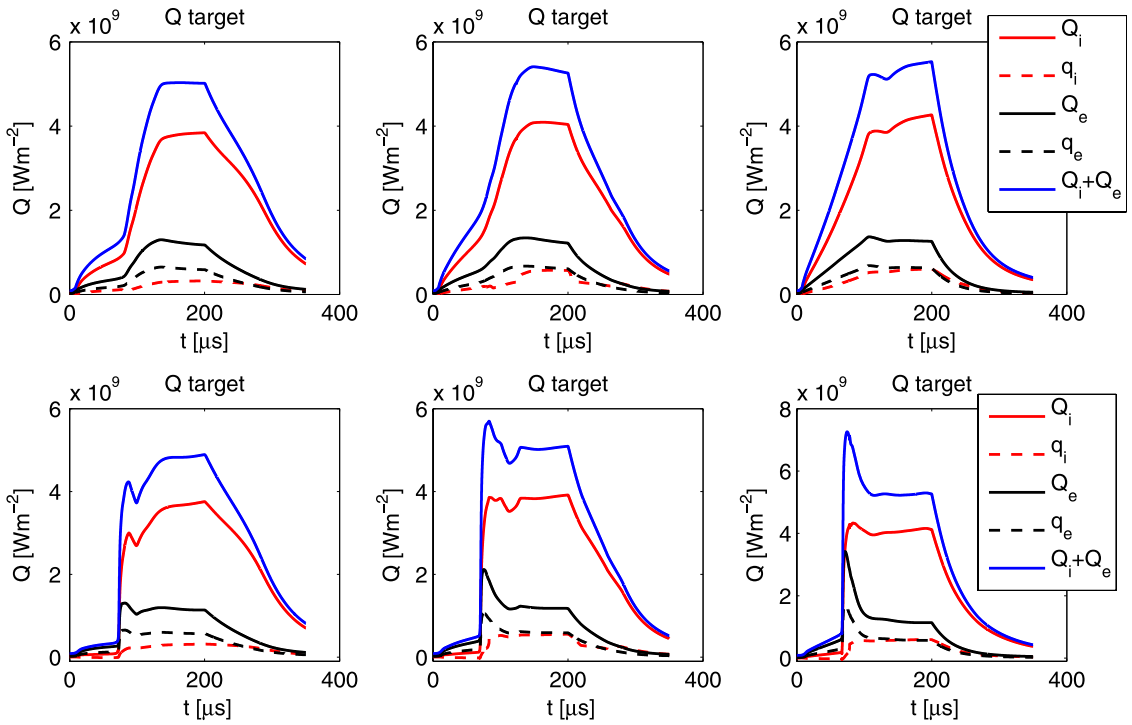

Figure 13. Parallel target energy flux modelled by the fluid code for (top) the reference convective ELM (left), a case when the radial source is equally shared by convection and conduction (middle) and a purely conductive ELM (right). The same for the bottom panels, but applying heat flux limiters $\alpha_e = 0.5$, $\alpha_i = 1.0$.

the target. Shaping of the source temporal profile influences neither the time scale nor the maximum target flux if the source amplitude and duration (and the total input energy) are the same. Inclusion of recycling at the targets, in contrast, affects the time scale. Figure 12 compares two solutions of the fluid code. While the duration of the source translates well to the duration of the increased target energy flux for the case without neutrals, slowing down effect of neutrals leads to broadening of the profile in time, which becomes more similar to what is observed experimentally (typical decay on the time scale of $\sim$1000 μs, see [25]). The effect of neutrals is included via a simple one-dimensional fluid model for deuterium atoms (including charge exchange, ionization, recombination and excitation processes). The essential effect results from the background plasma that is matched to the pre-ELM profile for the case without neutrals at the upstream position, but in addition, it involves recycling and ionization zones close to the targets, which interact with plasma of the ELM.

Further in this section, the SOLF1D code is used to study transients which are not purely convective. Ideally, we would like to estimate the energy source from the energy conservation equation similarly as we approximated the particle source using the continuity equation. It is, however, not so straightforward to parametrize energy losses due to conduction, see more in appendix. In this section we focus on how the energy flux evolution at the target is influenced if the ELM source is partly or, in the extreme case, fully conductive, i.e. $S_E > 3kT_{\rm ped}S_n$, which is practically done by a reduction of the particle source S_n for the same energy source S_E. Alternatively, we could investigate a situation with the same particle source S_n while increasing S_E. An extended study for conductive ELMs follows in the appendix.

The reference case described in section 3.1 ($n_{\rm ped} = 5 \times 10^{19}\,{\rm m}^{-3}$, $T_{\rm ped} = 1.5\,{\rm keV}$, $t_{\rm ELM} = 200\,\mu{\rm s}$) is used to illustrate the effect. In addition to this case shown in figure 13 on the left in the top row (i), we consider two situations with the same total energy input: (ii) a case when the ELM energy is equally shared by convection and conduction (middle) and (iii) a case of purely conductive ELM with no particle source (right), $S_n \approx 0$ (in fact S_n is equal to the pre-ELM value):

(i) $S_n = S_n^{\rm ref}$
(ii) $S_n = 0.5 S_n^{\rm ref}$
(iii) $S_n \approx 0$

and $S_E = S_E^{\rm ref}$ for all three cases, $S_E^{\rm ref} = 3kT_{\rm ped}S_n^{\rm ref}$. The convective (left) and half-conductive (middle) cases are comparable in amplitudes of the energy flux and do not reveal significant discrepancies, in addition to a slightly stronger increase in the target energy flux in the first phase. In the time trace of purely conductive transient (right), we note even stronger modification of the early phase which is governed by the heat conduction and we see a sharp immediate rise of the energy flux, but only 10% change in amplitude. The bottom panels show the effect of heat flux limiters for three studied transients. Both electron and ion energy fluxes are suppressed in the first period of transients when heat conduction occurs, which is followed by peaks of the energy flux right after. For conductive transients (middle and right), it is mainly a modification of the electron energy flux causing the sharp peaking of the total energy flux at the target. In the initial phase, conductive transport dominates, while later ∇T is very small and the conductive transport is reduced (see details in figure 19). Additionaly, heat flux limiters have no effect if

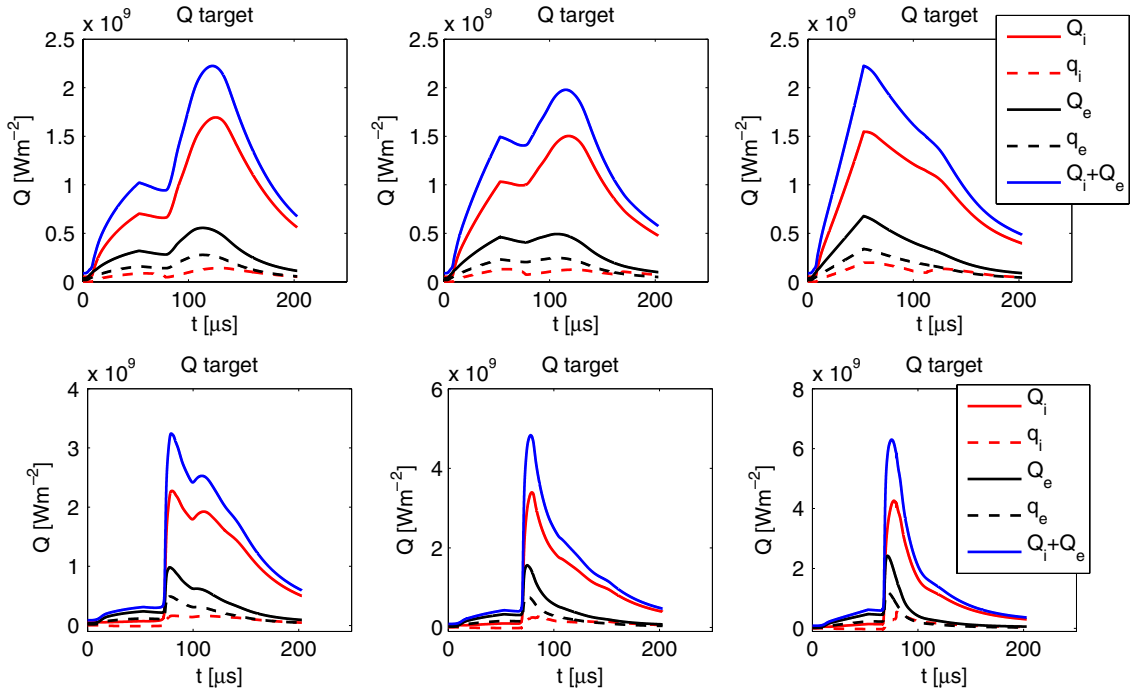

Figure 14. Parallel target energy flux modelled by the fluid code for: (top left) a convective 53 μs ELM, (top middle) a case when the radial source is equally shared by convection and conduction, (top right) a purely conductive ELM. In the bottom row, the same with applied heat flux limiters $\alpha_e = 0.5$, $\alpha_i = 1.0$.

$\nabla T \approx 0$. This also implies that the importance of conduction and heat flux limiters is bigger for shorter transients.

For a shorter (weaker) ELM ($t_{ELM} < \tau_\parallel$), introducing a conductive source can result in a strong modification of temporal profiles seen at the target. The conduction contribution in the target energy flux is more important for short transients (section 3.4) and it is even larger if we also further assume that the transient source has both convection and conduction components. This is demonstrated in figure 14, again with an artificial case of a purely conductive ELM that carries no source of particles and heats up the existing SOL plasma only. Relative change in the energy flux amplitude is again within 10% if the source is conductive. Bottom panels show the effect of heat flux limiters as in the previous case. In figure 14 (top), we can clearly identify two structures on different time scales, the early one due to conduction (weaker in PIC and Vlasov simulations, see figures 6–8) and the second one due to convection, where we find a fair agreement between the codes. Therefore, we would think that to match results obtained by fluid and kinetic modelling closer, it is desirable to use heat flux limiters which would reduce heat conduction and eliminate the structure which is observed at the target before 80 μs. One must be, however, careful with limiting the heat conductivity and no universal guide yet exists (see, e.g., [12, 17]). In figure 14 (bottom), it appears that the application of the heat flux limiters reduces the conductive transport substantially, but in contrast to kinetic simulations also increases the peak energy flux. Switching on the heat flux limiters leads to an increase in the energy flux by 46% (convective ELM) up to 183% (conductive ELM). At this stage, we do not have a PIC simulation for conductive ELMs for comparison. The conductive source was not further considered in BIT1 because a good quantitative agreement with experiment was achieved for the convective source. It is envisioned that the two techniques (kinetic and fluid) would move apart more expressly if a non-negligible fraction of the power is deposited at the target due to heat conduction. This can be the case when the energy source into the SOL due to the ELM is largely conductive and when the ELM crash is short compared with the parallel transport time scale $\tau_\parallel$ (e.g. represented as an impulse). Accurate models of heat flux limiters would be required taking into account time evolution and a benchmark with the PIC code would be beneficial.

Several additional cases (e.g. figures 15 and 16), for which we have a comparison with the PIC code, were performed with several values of heat flux limiters for electrons and ions separately. In figures 15 and 16 (convective transients), we see only a little influence of the electron heat flux limiter on the electron energy flux. In contrast, the ion energy flux (but also the electron energy flux) is sensitive to the change in the ion heat flux limiter. In figure 15 (longer duration of the transient), the best agreement with PIC is achieved when no heat flux limiters are employed. In figure 16 (shorter transient), the situation is different. We see again sharp peaks in the energy flux as soon as the convective energy transfer appears, but in addition, we can note, from comparing the energy fluence between the PIC and fluid codes, that the total power arriving at the target during the transient is larger in the PIC simulation. This indicates that the contribution of the background plasma in the total target energy flux (the first structure that appears in the PIC code due to reaction of background plasma to fast ELM particles) cannot be neglected, if the transient is short enough. A general conclusion concerning heat flux limiters resulting from performed simulations here is that spatially uniform and

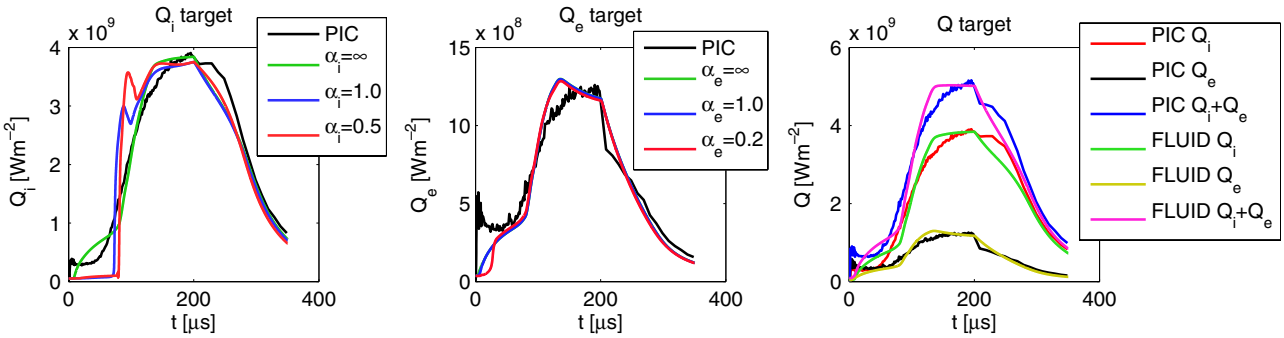

Figure 15. The effect of heat flux limiters on the parallel target energy flux for the reference case where parallel convective transport dominates: (left) ion energy flux in the PIC simulation compared with the fluid model using ion heat flux limiters $\alpha_i = \infty$ (no heat flux limiting), $\alpha_i = 1.0$, $\alpha_i = 0.5$, (middle) electron energy flux in the PIC simulation compared with the fluid model using electron heat flux limiters $\alpha_e = \infty$, $\alpha_e = 1.0$, $\alpha_e = 0.2$, (right) comparison of PIC and fluid results without heat flux limiters.

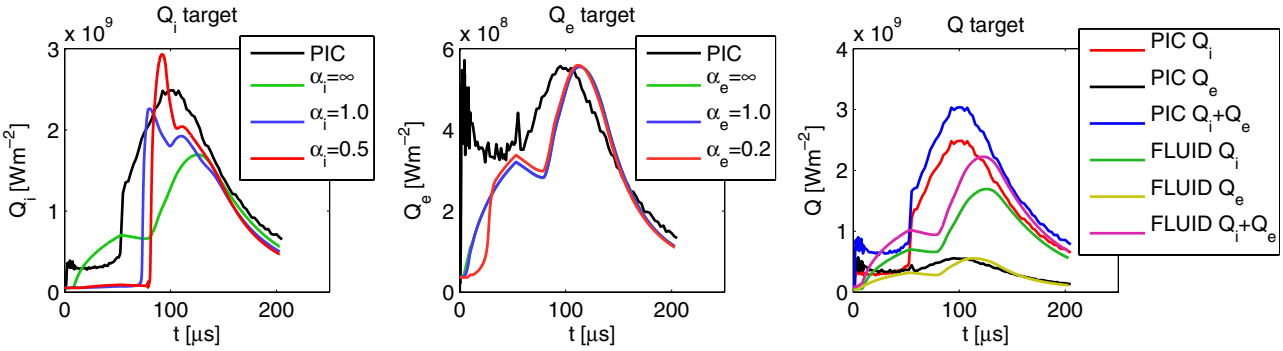

Figure 16. The same as in figure 15, but for a short transient of 53 μs where parallel conductive transport is important and the kinetic and fluid techniques start to disagree. Note that in the PIC simulation, we observe larger total time-integrated flux $\epsilon_\parallel$ than in the fluid code by a factor of 1.24. It is because the thermal background plasma in the PIC simulation contributes to the total target energy flux as the ELM pulse pushes the plasma towards the divertor and in the case of a short (small) transient, this contribution is not negligible.

especially constant in time limiting factors do not improve agreement with the PIC simulation and a systematic study would be necessary. The temporal variation of the heat flux limiting factors during a transient is demonstrated by a kinetic simulation in [17].

Implications of one-dimensional results for conductive ELMs (ITER case) could be summarized as follows. Generally, the power response at the target is a function of the upstream source. This source is linked to perpendicular transport of particles and energy and to physics of the ELM crash in the pedestal and its determination is not trivial. However, for a given energy source, we observe the same peak energy flux $Q_\parallel^{\max}$ irrespective of the parallel transport process. The main transport processes (convection/conduction) are reflected in the profiles of target energy fluxes on different time scales, which are clearly separated especially for short transients. The role of transient duration is in affecting the importance of parallel conduction. Further, a parameter that influences $Q_\parallel^{\max}$ in the fluid modelling is the heat flux limiter, with a large effect during short transients, but a small effect for long transients with $t_{\rm ELM} > \tau_\parallel$ (i.e. in the case of ITER for $t_{\rm ELM} > 200$ s).

6. Conclusions

Parallel transport in the SOL in response to the ELM crash is modelled and three numerical techniques are benchmarked. Even though kinetic effects are evident in results of PIC and Vlasov simulations, fluid modelling shows a satisfactory agreement with the kinetic approach. It appears that an instant response at the target due to fast ELM electrons, not captured in the fluid code, does not contribute substantially to the total deposited power. The main contribution is dominated by ion dynamics and energy convection. For typical conditions experimentally observed at JET, a fluid code (SOLF1D) describes reasonably well the main features of the transient's parallel propagation and predicts approximately the same peak energy flux at the target and similar time histories of the parallel energy flux as a PIC model (BIT1) and a model based on the Vlasov equation.

Assuming a one-dimensional problem and neglecting the effect of neutrals or impurities, expressions for the energy fluence parallel to the magnetic field $\epsilon_\parallel \approx 0.56 p_{\rm ped} c_{\rm s,ped} t_{\rm ELM}$ and the parallel peak energy flux at the target $Q_\parallel^{\max} \approx 0.55 p_{\rm ped} c_{\rm s,ped} \min\{1, t_{\rm ELM}/\tau_\parallel\}$ are derived from simulation results (at constant $L_{\rm s}/L_\parallel$) and compared between the codes. These fits follow from assumptions of convective ELMs and approximate link between parallel and perpendicular transport resulting in an estimate of the source into the SOL, $S_n \sim n_{\rm ped} c_{\rm s,ped}/L_{\rm s}$. All three codes show the same characteristics of the obtained scalings. Only the Vlasov model gives slightly lower $Q_\parallel^{\max}$ which is proved in [23] to be caused by no collisions included in the model and hence missing collision-based diffusive heat transport. Finally, predictions

for ITER are drawn from these fits, leading to the total energy density deposited at the target in the parallel direction $\epsilon_\parallel \approx 7.44\,\mathrm{MJ\,m^{-2}}$ and the amplitude $Q_\parallel^{\max} \approx 36.52\,\mathrm{GW\,m^{-2}}$ for an ELM crash of 200 μs with $n_{\mathrm{ped}} = 6 \times 10^{19}\,\mathrm{m^{-3}}$ and $T_{\mathrm{ped}} = 5\,\mathrm{keV}$. The corresponding poloidal fluence and flux are $\epsilon_{\mathrm{pol}} \approx 0.52\,\mathrm{MJ\,m^{-2}}$ and $Q_{\mathrm{pol}}^{\max} \approx 2.55\,\mathrm{GW\,m^{-2}}$ for $\alpha_{\mathrm{t}} = 4^\circ$ between parallel and poloidal directions or $\epsilon_\perp \approx 0.32\,\mathrm{MJ\,m^{-2}}$ and $Q_\perp^{\max} \approx 1.59\,\mathrm{GW\,m^{-2}}$ for field line angle at the target $\alpha = 2.5^\circ$.

Additional questions such as the effect of heat conduction in the energy source into the SOL during the ELM crash or heat flux limiters are discussed on the basis of fluid results. $Q_\parallel^{\max}$ does not change for the same energy source distributed differently between convection and conduction if $t_{\mathrm{ELM}} > \tau_\parallel$. For $t_{\mathrm{ELM}} < \tau_\parallel$, $Q_\parallel^{\max}$ is sensitive to application of heat flux limiters and a comparison of fluid and kinetic codes for conductive transients would be useful.

Few assumptions are made in the fluid code—fractions of the input power carried by ions and electrons are modified, the viscosity limiter is applied, while in contrast it turns out that employing heat flux limiters does not necessarily give better results (better match is obtained with no heat flux limiters than with limiters constant in time). Only for largely conductive (very low ν_{e}^*) and short ELMs ($t_{\mathrm{ELM}} < \tau_\parallel$), is a departure between the codes anticipated. Results show that the validity of the fluid model is disputable if the heat conduction plays the major role in the power deposition at the target. These findings can be considered in two-dimensional SOL transport solvers.

Earlier, results of the PIC model for JET type I ELMs were successfully compared with measurements in [12, 16] and a comparison in [25] demonstrated agreement between free-streaming model and IR data for the shape of a heat pulse in time. However, the derived expressions for $\epsilon_\parallel$ and $Q_\parallel^{\max}$, which involve pedestal quantities, have to date not been compared with experiment and a comparison with IR data from the AUG and JET tokamaks is planned.

In the last paragraph, we present several results from the appendix which separate the paper, with main aim to compare fluid and kinetic models, from an additional analysis carried out with the fluid model exclusively, focusing more on description of conductive transients. The reader is referred to the appendix for more details. Regarding the fact ELMs are conductive for lower collisionalities (as in ITER), it is interesting to see that a parametrization of $\epsilon_\parallel$ and $Q_\parallel^{\max}$ with upstream SOL quantities for both convective and conductive transients shows a similar functional form as the fits above for convective ELMs, however, with p and c_{s} measured in the upstream SOL instead of the pedestal (one-dimensional situation only). Further, convective and conductive parallel energy losses calculated by the fluid code reveal the same collisionality dependence as experimental pedestal energy losses. Finally, the ratio between the SOL size and the size of the ELM affected area in the pedestal $R_{\mathrm{SOL}}/R_{\mathrm{ped}}$ is estimated from a simple one-dimensional analysis, credibility of which should be proven/disproven by comparison with 2–3D models including more complex transport. The ratio scales as $R_{\mathrm{SOL}}/R_{\mathrm{ped}} \approx \pi^2 a\sqrt{\kappa}/(L_{\mathrm{s}} \sin\alpha_{\mathrm{u}})$ for convective ELMs and for purely conductive ELMs ($\Delta n_{\mathrm{ped}} \approx 0$), this is multiplied by $\tau_\parallel^n/\tau_\parallel^T$, provided that $\epsilon_\parallel$ scales with $p_{\mathrm{ped}} c_{\mathrm{s,ped}} t_{\mathrm{ELM}}$.

Acknowledgments

This work was supported by EURATOM and carried out within the framework of the European Fusion Developlment Agreement. The views and opinions expressed herein do not necessarily reflect those of the European Commission. The CCFE authors were funded by the RCUK Energy Programme under grant EP/G003955. DT acknowledges support of projects FWF P21941-N16, GNSF/ST09_305_4-140. GM thanks INRIA Nancy Grand-Est (CALVI project) for partial financial support.

Appendix

Parallel losses modelled by SOLF1D

Detailed analysis of parallel losses and fluxes for the reference case from section 3.1 is presented in figures 17–20. A similar study has been done in [9] for a transient in high-recycling SOL corresponding to a typical turbulent blob. Figure 17 displays parallel particle and energy losses due to convective and conductive processes (loss terms $S_\parallel^n$ and $S_\parallel^E$ are evaluated upstream at the outboard midplane) and the midplane density and temperatures. The density goes up to $n \approx 5.5 \times 10^{19}\,\mathrm{m^{-3}}$, about the pedestal density $n_{\mathrm{ped}} = 5 \times 10^{19}\,\mathrm{m^{-3}}$. For the energy source distributed as $S_{E,\mathrm{i}}/S_{E,\mathrm{e}} = 3$ and calculated as $S_E = 3kT_{\mathrm{ped}}S_n$ with $T_{\mathrm{ped}} = 1500\,\mathrm{eV}$, the temperatures upstream reach $T_{\mathrm{i}} \approx 1125\,\mathrm{eV}$ and $T_{\mathrm{e}} \approx 251\,\mathrm{eV}$ at 200 μs (lower than the temperature prescribed to the source).

Figures 18 and 19 show parallel fluxes at the target ($x = -L_\parallel$) and at the position corresponding to the source end ($x = -L_{\mathrm{s}}/2$). Parallel profiles of the density, velocity and temperature during the transient are displayed in figure 20. The temperatures show almost no gradients (sheath-limited regime and flattening due to prompt heat diffusion), while the density is governed by convective transport with gradient length scale of the source size L_{s}, see peaking of the velocity (visible on the red curve) and the density structure with two (less visible) peaks (green curve) corresponding to the pulse location.

Although conductive energy losses are strong on very short time scales (figure 17, blue), their total contribution to parallel losses during the transient is for electrons comparable to convective losses and for ions roughly four times smaller than convective losses (small temperature gradients). For very short transients, their total contribution would be dominant, but in this case (and in general if $t_{\mathrm{ELM}} > \tau_\parallel$), losses at 200 μs (almost steady state) are more relevant in describing the total energy loss during the transient. Parallel fluxes in figure 19 (calculated at the source edge) reveal the same structure as parallel losses calculated at the midplane. A similar picture is also obtained for half-conductive and fully conductive transients from figure 13, though not surprisingly with lower/higher convection/conduction contributions. The target fluxes in figure 18 are governed by imposed boundary conditions, that is why $q_{\parallel,\mathrm{e}} = Q_{\parallel,\mathrm{e}}^{\mathrm{kin}}$. The particle flux at the target, $x = -L_\parallel$, copies the flux seen at the end of the source, $x = -L_{\mathrm{s}}/2$. The energy flux profile between these two locations is modified along the distance $L_\parallel$ (while the pulse

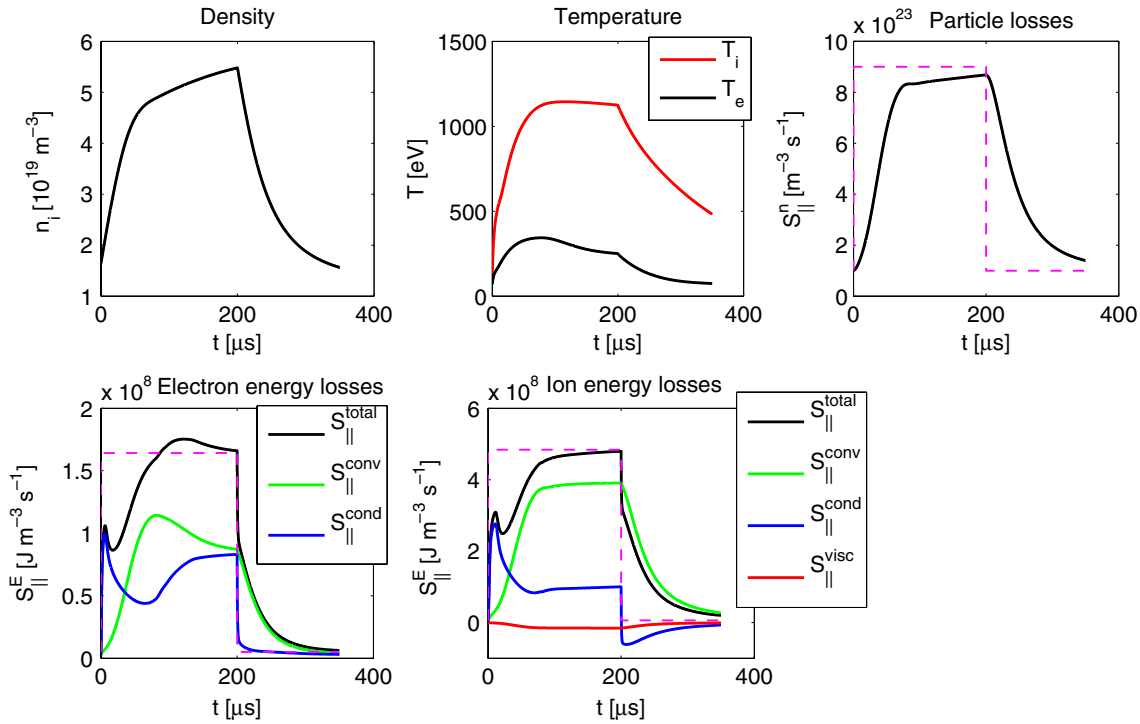

Figure 17. Plasma parameters upstream (outboard midplane) during the transient—(top left) plasma density n, (top middle) plasma temperature T_e and T_i, (top right) parallel particle losses $S_\parallel^n = \partial/\partial x(nv_\parallel)$, (bottom left) parallel electron energy losses $S_\parallel^E$ and individual components $S_\parallel^{conv} = \partial/\partial x(5/2nkT_e v_\parallel)$, $S_\parallel^{cond} = \partial/\partial x[-\kappa_{\parallel,e}\partial/\partial x(kT_e)]$, (bottom right) parallel ion energy losses $S_\parallel^E$ and components $S_\parallel^{conv} = \partial/\partial x(5/2nkT_i v_\parallel + 1/2m_i n v_\parallel^3)$, $S_\parallel^{cond} = \partial/\partial x[-\kappa_{\parallel,i}\partial/\partial x(kT_i)]$, $S_\parallel^{visc} = \partial/\partial x[-v_\parallel \eta_{\parallel,i}\partial v_\parallel/\partial x]$, see equations (4)–(7). The dashed purple line is the source.

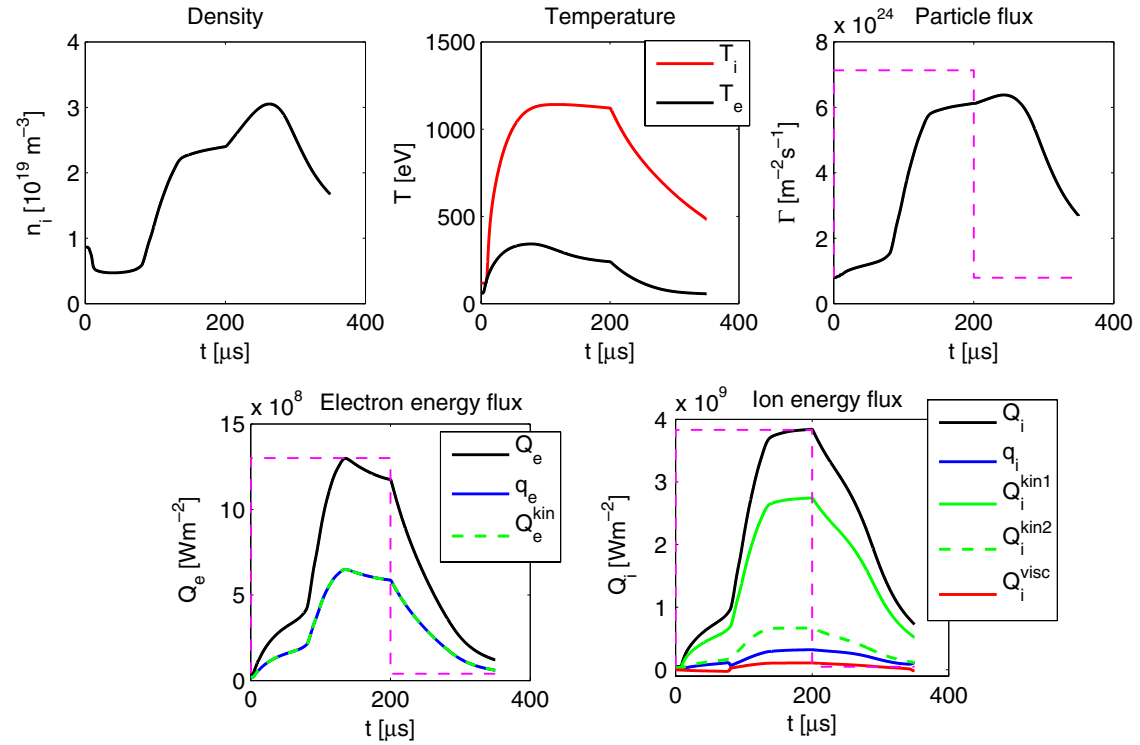

Figure 18. Plasma parameters at the target during the transient—(top left) plasma density n, (top middle) plasma temperature T_e and T_i, (top right) parallel particle flux $\Gamma_\parallel = nv_\parallel$, (bottom left) parallel electron energy flux $Q_{\parallel,e}$ and individual components $q_{\parallel,e} = -\kappa_{\parallel,e}\partial/\partial x(kT_e)$, $Q_{\parallel,e}^{kin} = 5/2nkT_e v_\parallel$, (bottom right) parallel ion energy flux $Q_{\parallel,i}$ and components $q_{\parallel,i} = -\kappa_{\parallel,i}\partial/\partial x(kT_i)$, $Q_{\parallel,i}^{kin1} = 5/2nkT_i v_\parallel$, $Q_{\parallel,i}^{kin2} = 1/2m_i n v_\parallel^3$, $Q_{\parallel,i}^{visc} = -v_\parallel \eta_{\parallel,i}\partial v_\parallel/\partial x$.

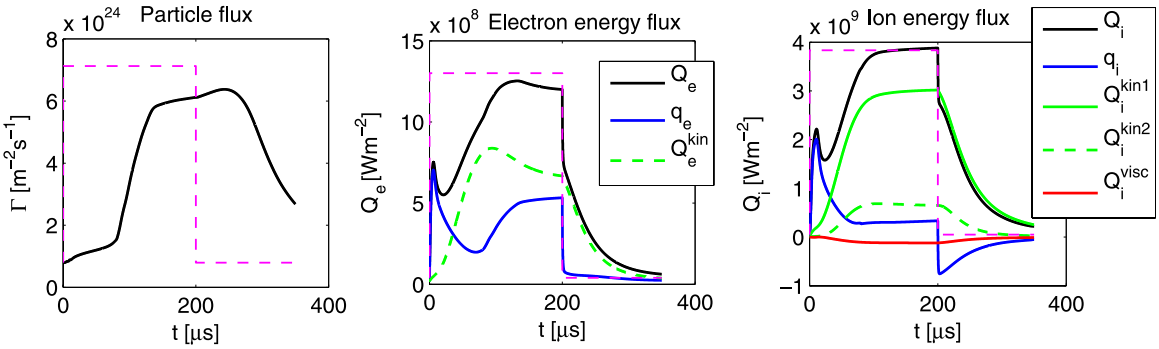

Figure 19. Particle and energy fluxes as in figure 18, now not at the target, but at the edge of the source.

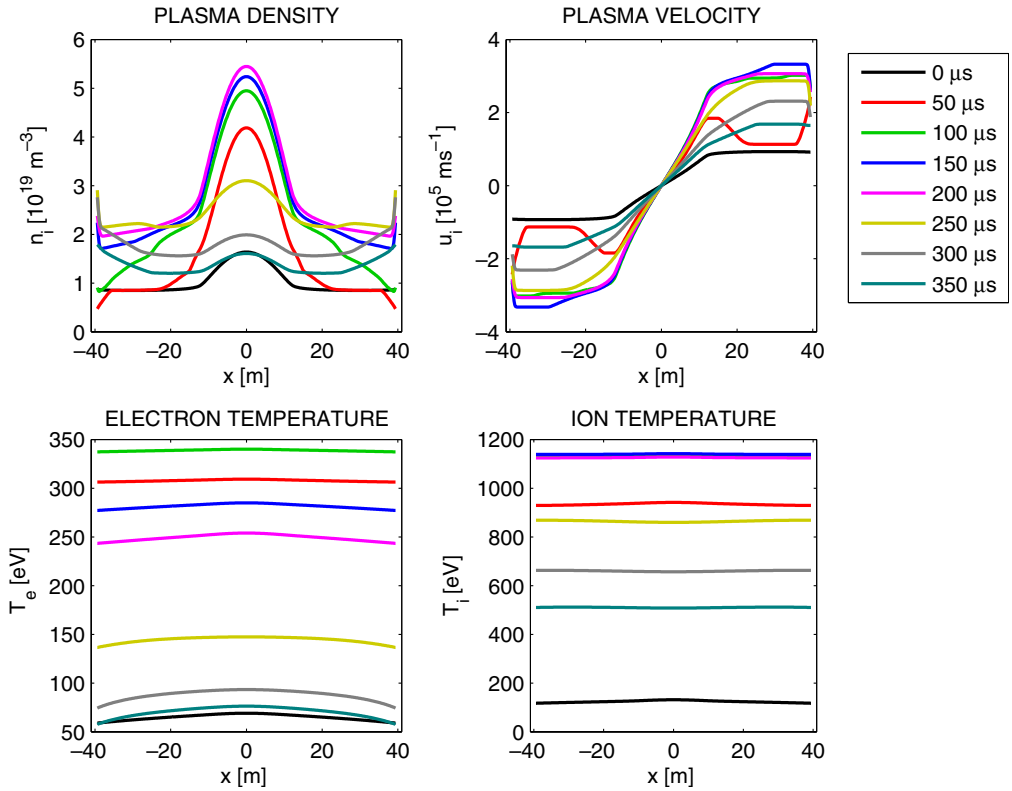

Figure 20. Snapshots of parallel profiles during the transient taken each 50 μs. The transient lasts for 200 μs.

travels towards the target, heat diffusion is removing energy from the pulse and flattening the temperature gradients), but the peak values are comparable.

Series of transients are analysed, with energy sources including both convective and conductive components. One scan is done over the particle source S_n, reducing S_n for a fixed energy source S_E and the second scan is with varying S_E for a fixed S_n (table 5). The duration is 200 μs in all cases. The aim of the study is to investigate parallel transport for conductive ELMs and look at dependences of target quantities similarly as in the study of convective ELMs, equations (19) and (23). Quantities in the following figures are displayed as functions of plasma parameters upstream (midplane, separatrix) instead of pedestal values, as the link between pedestal and upstream locations is missing in the one-dimensional code. Therefore the study provides an insight into the parallel transport only.

Table 5. Particle and energy sources included in the scan. The first transient is the reference convective case with $T_{\rm ped} = 1500$ eV, $n_{\rm ped} = 5 \times 10^{19}$ m^{-3}, $S_E^{\rm ref} = 3kT_{\rm ped}S_n^{\rm ref}$ and $S_n^{\rm ref} \approx An_{\rm ped}c_{\rm s,ped}/L_{\rm s}$. $S_{E,\rm i}/S_{E,\rm e} = 3$ in all cases.

(1)	$S_n = S_n^{\rm ref}$	$S_E = S_E^{\rm ref}$
(2)	$S_n = 0.5S_n^{\rm ref}$	$S_E = S_E^{\rm ref}$
(3)	$S_n = 0.2S_n^{\rm ref}$	$S_E = S_E^{\rm ref}$
(4)	$S_n \approx 0$	$S_E = S_E^{\rm ref}$
(5)	$S_n = S_n^{\rm ref}$	$S_E = 1.5S_E^{\rm ref}$
(6)	$S_n = S_n^{\rm ref}$	$S_E = 2.0S_E^{\rm ref}$
(7)	$S_n = S_n^{\rm ref}$	$S_E = 3.0S_E^{\rm ref}$
(8)	$S_n = S_n^{\rm ref}$	$S_E = 5.0S_E^{\rm ref}$

In figure 21, normalized parallel density and temperature losses $S_\parallel^n/n$ and $S_\parallel^T/T$ are plotted as functions of upstream parameters. These losses are calculated at $t = 200\,\mu$s not far from steady state, i.e. describe well the total losses over the

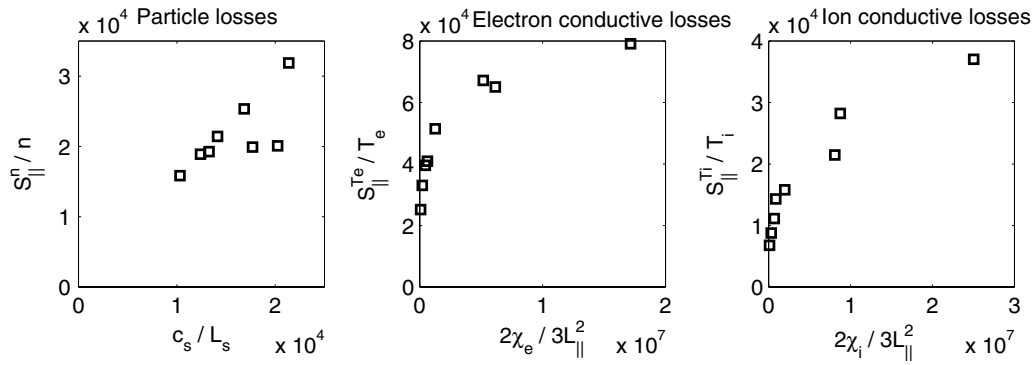

Figure 21. Particle losses $S^n_\parallel = \partial/\partial x(nv_\parallel)$ and temperature losses $S^T_\parallel$ (only the conductive part $S^{T,\mathrm{cond}}_\parallel = 2/(3kn)\partial/\partial x[-\kappa_\parallel \partial/\partial x(kT)]$) evaluated at the upstream location as functions of upstream parameters.

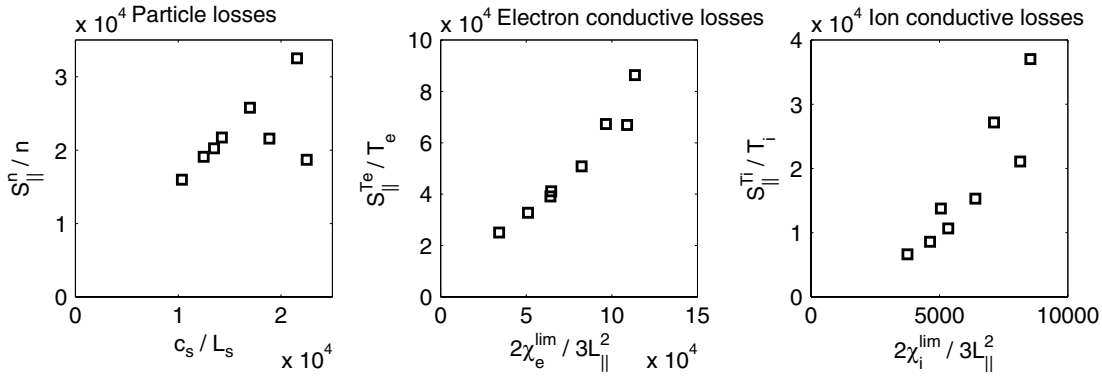

Figure 22. Parallel losses as functions of upstream parameters as in figure 21, but with heat flux limiters $\alpha_\mathrm{e} = 0.5$, $\alpha_\mathrm{i} = 1.0$.

period of the transient because of $t_\mathrm{ELM} > \tau_\parallel$. As a consequence of long enough duration, parallel losses are related to radial sources as $S^n_\parallel \approx S_n$ and $S^E_\parallel \approx S_E$. Figure 21 (left) shows that the factor $nc_\mathrm{s}/L_\mathrm{s}$ calculated upstream seems to be a good measure of particle losses $S^n_\parallel$ and $S^n_\parallel \approx 1.5nc_\mathrm{s}/L_\mathrm{s}$. There are two points which deviate from the linear scaling. These points correspond to cases 3 and 4 in table 5 and differ from the others by effectively no particle source during the transient, the upstream density is even decreasing during the pulse (deviation of these points from the linear trend is not visible if plotted as $S^n_\parallel$ over $nc_\mathrm{s}/L_\mathrm{s}$). In figure 21 (right), there is an ordering of the conductive temperature losses $S^T_\parallel$ with upstream $2\chi_\parallel T/3L^2_\parallel$, although not linear and absolute values do not agree ($\chi_\parallel = \kappa_\parallel/n$ and defined by Braginskii formula). $L_\parallel$ or L_s are smaller than the typical gradient temperature length (almost no temperature gradients), while parallel heat conductivities ($\sim T^{5/2}$) are very high (see figure 20). A scan from table 5 is repeated with heat flux limiters and results are shown in figure 22. The absolute values of parallel loss factors are not changed much, because conductive losses are reduced by the application of heat flux limiters only in very early phase of the transient when there is still some temperature gradient along the field line. However, quantitative agreement of the parametrization is better than in the previous case without limiters. The reason is that we plot data over modified heat diffusivities $\chi^\mathrm{lim}_\parallel$ taking into account the effect of heat flux limit, $\chi^\mathrm{lim}_\parallel = \chi_\parallel(1 + \chi_\parallel/\alpha L_\parallel v_\mathrm{th})^{-1}$.

The energy fluence at the target $\epsilon_\parallel$ (as well as the total energy losses) scales with the upstream value of $pc_\mathrm{s}t_\mathrm{ELM}$ (figure 23) as

$$\epsilon_\parallel \approx 1.7 pc_\mathrm{s}t_\mathrm{ELM} \tag{25}$$

where $p = nk(T_\mathrm{e} + T_\mathrm{i})$ and $c_\mathrm{s} = \sqrt{k(T_\mathrm{e} + T_\mathrm{i})/m_\mathrm{i}}$. The peak energy flux at the target is approximately $Q^\mathrm{max}_\parallel \approx \epsilon_\parallel/t_\mathrm{ELM}$. The second scan with heat flux limiters (magenta crosses) shows similar trends as the scan without limiters (black squares), only somewhat higher $Q^\mathrm{max}_\parallel$ for the most conductive pulses. The coefficient 1.7 is higher than in the dependence found previously, equation (19). For the same convective transient as in section 3.1, the temperatures in the upstream SOL do not reach the pedestal temperature used in section 3.1 to define the particle and energy sources, due to cooling by conductive heat transport during the transient. That is the reason why $pc_\mathrm{s}t_\mathrm{ELM}$ evaluated upstream is a factor of 3 smaller than $p_\mathrm{ped}c_\mathrm{s,ped}t_\mathrm{ELM}$ used in equation (19). The fits for $\epsilon_\parallel$ and $Q^\mathrm{max}_\parallel$ call for a comparison with experiment or for a similar study in two dimensions which would cover the link between the pedestal and separatrix locations and include two-dimensional processes in the SOL.

Figure 24 shows the dependence of parallel losses on the upstream electron collisionality and $\tau_\parallel$ (left and middle) and total parallel energy losses for electrons and ions with convective part separately. The collisionality is defined as $\nu^* = L_\parallel/\lambda_\mathrm{ee}$ with $\lambda_\mathrm{ee} = 1.2 \times 10^{16} T^2_\mathrm{e}/n$. If $S^n_\parallel \approx \Delta n_\mathrm{ped}/t_\mathrm{ELM}$ and $S^T_\parallel \approx \Delta T_\mathrm{ped}/t_\mathrm{ELM}$ is assumed, $\Delta\epsilon/\epsilon$ from figure 24 can be related to $\Delta W_\mathrm{ELM}/W$ (see next section). In figure 24, we see that the one-dimensional parallel transport model reproduces typical dependences observed

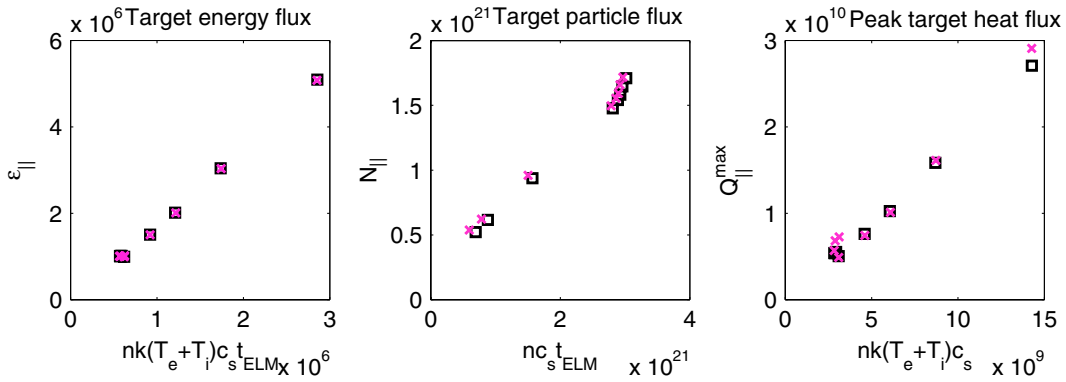

Figure 23. Target quantities $\epsilon_\parallel$, $n_\parallel$ and $q_\parallel^{\max}$ as functions of upstream parameters. one scan without heat flux limiters (black squares), second scan with heat flux limiters $\alpha_e = 0.5$, $\alpha_i = 1.0$ (magenta crosses).

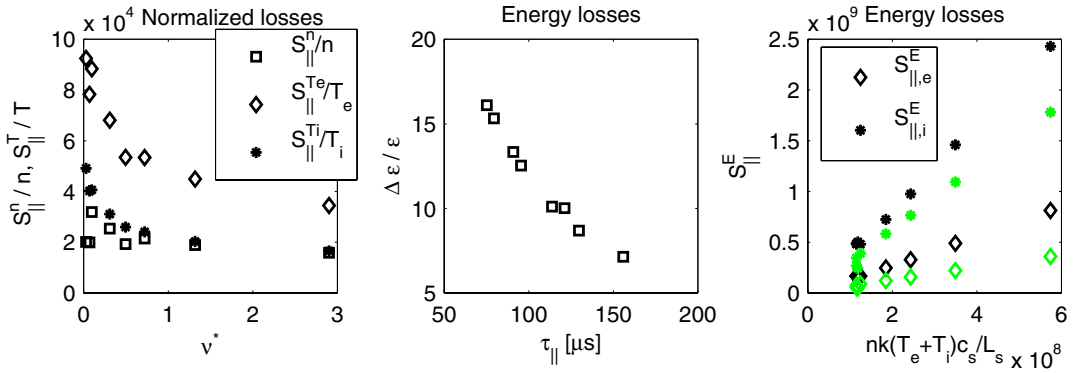

Figure 24. Normalized parallel losses $S_\parallel^n/n$, $S_\parallel^{Te}/T_e$ and $S_\parallel^{Ti}/T_i$ (total temperature removal terms including convective, conductive and visous losses) on the left, n, T_e and T_i are upstream values. In the middle, losses in terms of $\Delta\epsilon/\epsilon$ where $\Delta\epsilon = \frac{3}{2}k[nS_\parallel^{Te} + nS_\parallel^{Ti} + (T_e + T_i)S_\parallel^n]t_{ELM}$ and $\epsilon = \frac{3}{2}nk(T_e + T_i)$. On the right, total energy losses $S_\parallel^E$ for electrons and ions separately (black) and convective part of losses $S_\parallel^{E,conv} = \partial/\partial x(5/2nkTv_\parallel)$ (grey/green).

experimentally [28, 30]. Convective losses are less sensitive to the collisionality than conductive losses and electron conductive losses dominate over the ion ones due to faster cooling.

Parallel and perpendicular balance during the ELM crash

The total energy lost from the pedestal into the SOL during the ELM crash can be expressed from measurements as

$$\Delta W_{ELM} = \int \Delta\left[\frac{3}{2}n_{ped}k(T_{e,ped} + T_{i,ped})\right]\mathrm{d}V \approx \Delta(3n_{ped}kT_{ped})V_{ped} \quad (26)$$

where V_{ped} is the volume in the pedestal corresponding to the ELM affected area, $V_{ped} \approx 2\pi a\sqrt{\kappa}2\pi R\Delta R_{ped}$ and ΔR_{ped} is the corresponding characteristic pressure width in the pedestal. Let us define the radial width as $\Delta R_{ped} = \int \Delta p_{ped}\mathrm{d}r/\Delta p_{ped}^{\max}$, $T_{ped}\Delta n_{ped}\Delta R_{ped}^n + n_{ped}\Delta T_{ped}\Delta R_{ped}^T = \Delta(n_{ped}T_{ped})\Delta R_{ped}$.

We distinguish between losses due to convection and conduction given by pedestal density and temperature drops, respectively

$$\Delta W_{ELM} \approx 3k(T_{ped}\Delta n_{ped} + n_{ped}\Delta T_{ped})V_{ped}. \quad (27)$$

If the temperature drop is small, convective losses dominate (though figure 9 in [28] shows it is often not the case) and we can assume

$$\Delta W_{ELM} \approx 3kT_{ped}\Delta n_{ped}V_{ped} \approx 2\pi a\sqrt{\kappa}2\pi R\Delta R_{ped}3kT_{ped}\Delta n_{ped}. \quad (28)$$

One of the interpretations for explaining observed dependences of ΔW_{ELM} on the pedestal collisionality is that plasma in the pedestal connects with the targets during MHD activity due to changes of the magnetic field structure. Then the pedestal pressure is thought to be reduced by parallel transport in the SOL. See, e.g., [28] or [29], where a crude approximation linking radial transport with parallel losses is used

$$\frac{\mathrm{d}n_{ped}}{\mathrm{d}t} \approx \frac{\Delta n_{ped}}{t_{ELM}} \approx S_\parallel^n \approx -\frac{n_{ped}}{\tau_\parallel^n},$$
$$\frac{\mathrm{d}T_{ped}}{\mathrm{d}t} \approx \frac{\Delta T_{ped}}{t_{ELM}} \approx S_\parallel^T \approx -\frac{T_{ped}}{\tau_\parallel^T} \quad (29)$$

describing the density and temperature drops by parallel loss factors as

$$\frac{\Delta n_{ped}}{n_{ped}} \approx -\frac{t_{ELM}}{\tau_\parallel^n}, \qquad \frac{\Delta T_{ped}}{T_{ped}} \approx -\frac{t_{ELM}}{\tau_\parallel^T}. \quad (30)$$

Parallel loss times are often approximated as

$$\tau_\parallel^n \approx \frac{L_\parallel}{c_{s,ped}}, \qquad \tau_\parallel^T \approx \frac{3L_\parallel^2}{2\chi_{\parallel,e}}, \quad (31)$$

see equations (4)–(7), $\chi_{\parallel,e} = \kappa_{\parallel,e}/n_e$. This approximation is compared with experimental observations in [28] and it appears that it works well for the temperature (even though absolute values do not agree), while for convective losses, a clear dependence predicted by the model is not observed in experiment, figure 10 in [28]. If we compare the approximate expressions for removal times, we can derive that convective energy losses along the field line dominate over conductive losses for higher values of pedestal collisionality $\nu_e^* \sim L_\parallel n_{ped}/T_{ped}^2$. That is also confirmed by measurements in [28] or seen in JOREK simulations [21]. The expressions (31) can be compared with losses calculated in the fluid code (see figure 21). It was shown that parallel particle losses $S_\parallel^n$ can be parametrized by upstream nc_s/L_s, i.e. rather using the source length L_s instead of the connection length $L_\parallel$ as the typical parallel gradient length for the density. Parallel temperature losses $S_\parallel^T$ do not show a clear dependence on upstream $2\chi_\parallel T/3L_\parallel^2$, mainly due to almost zero temperature gradients along the field line during the transient (see figure 20).

The ELM energy from equation (27) can be equated to energy arriving at the target. Previously, we related the released energy ΔW_{ELM} for convective transients to the radial length where the energy is expelled in the SOL ΔR_{SOL}, equation (14). ΔW_{ELM} in this relation is consistent with the energy deposited at the target, equation (21). From equation (21) and using the fit for $\epsilon_\parallel$ (19), we obtain

$$\begin{aligned}\Delta W_{ELM} &\approx 2\pi R \Delta R_{SOL} \sin\alpha_u 2\epsilon_\parallel \\ &\approx 2\pi R \Delta R_{SOL} \sin\alpha_u \times 0.56 \times 4 n_{ped} k T_{ped} c_{s,ped} t_{ELM}.\end{aligned} \quad (32)$$

Comparison with ΔW_{ELM} estimated on the pedestal side, equation (27), leads to a relation between the lengths ΔR_{ped} and ΔR_{SOL}

$$\frac{\Delta R_{SOL}}{\Delta R_{ped}} \approx \frac{1}{0.56} \times \frac{3}{2}\left(\frac{\Delta n_{ped}}{n_{ped}} + \frac{\Delta T_{ped}}{T_{ped}}\right)\frac{\tau_{pol}}{t_{ELM}}\frac{1}{\sin\alpha_u} \quad (33)$$

where τ_{pol} is defined as $\tau_{pol} \equiv \pi a\sqrt{\kappa}/c_{s,ped}$.

Factors $\Delta n_{ped}/n_{ped}$ and $\Delta T_{ped}/T_{ped}$ can be estimated from experiment or approximated by a parametric dependence, e.g. (30). Experimental data in figure 3 in [28] show relative pedestal density and temperature drops $\Delta n_{ped}/n_{ped} \approx 0.3$ and $\Delta T_{ped}/T_{ped} \approx 0.5$ for a typical JET ELM. We estimated the radial size of the ELM affected area for this case as $\Delta R_{ped} \approx 10$ cm. The pedestal density and temperature drops approximately translate to relative pedestal energy losses as

$$\frac{\Delta W_{ELM}}{W} \approx \left(\frac{\Delta n_{ped}}{n_{ped}} + \frac{\Delta T_{ped}}{T_{ped}}\right)\frac{2\Delta R_{ped}}{a\sqrt{\kappa}}, \quad (34)$$

which gives convective losses of 4.6% and conductive losses of 8% for the ELM from figure 3 in [28] (assuming the same $\Delta R_{ped} \approx 10$ cm for both). The ELM energy losses are measured with respect to $W = 3n_{ped}kT_{ped}V_{plasma}$ and in (34), we approximated the plasma volume as $V_{plasma} \approx \pi a^2 \kappa 2\pi R$. Convective and conductive components of normalized energy losses $\Delta W_{ELM}/W$ for typical JET type I ELMs are shown in figure 9 in [28]. A scan over the electron collisionality gives a spread of conductive losses between 3% and 23% and convective losses relatively insensitive to ν_{ped}^* in the range 2–9%. From equation (33) and using $t_{ELM} \approx 200$ μs, $a \approx 1$ m, $\kappa \approx 1.7$ and $\sin\alpha_u \approx 0.25$, we get $\Delta R_{SOL}/\Delta R_{ped} \approx 0.58$, i.e. $\Delta R_{SOL} \approx 5.8$ cm. ΔR_{SOL} calculated from equation (33) reflects broadening compared with the inter-ELM values 3–7 mm reported in [4, 5], though it is larger than the typically observed SOL power width during ELMs 7–18 mm. In order to achieve comparable values of ΔR_{SOL} based on the simple estimate (33), the ELM crash duration t_{ELM} would have to be longer or the prefactor in equation (19) would have to be larger. Note that no neutrals or radiation is taken into account as well as no in/out asymmetry, while in experiment the asymmetry is in favour of the inner target. In addition, the energy fluence at the target in equation (19) is calculated for convective ELMs, i.e. the energy source in the SOL is approximated as $S_E \approx 3kT_{ped}n_{ped}c_{s,ped}/L_s$, while from experiment, we took into account both convective and conductive parts of pedestal losses.

If we assume convective ELMs ($\Delta T_{ped} \approx 0$) and replace $\Delta n_{ped}/n_{ped}$ in equation (33) by $t_{ELM}/\tau_\parallel^n$ according to (30), a simple analytic model for convective parallel losses (31) leads to mapping of the ELM affected area in the pedestal to the target wetted area as

$$\frac{\Delta R_{SOL}}{\Delta R_{ped}} \approx \frac{1}{0.56} \times \frac{3}{2}\frac{\tau_{pol}}{\tau_\parallel^n}\frac{1}{\sin\alpha_u} \approx \frac{1}{0.56} \times \frac{3\pi a\sqrt{\kappa}}{2L_\parallel \sin\alpha_u}. \quad (35)$$

This gives an estimate $\Delta R_{SOL}/\Delta R_{ped} \approx 1.1$ for JET ($\kappa \approx 1.7$, $a \approx 1$ m, $L_\parallel \approx 40$ m, $\sin\alpha_u \approx 0.25$) and $\Delta R_{SOL}/\Delta R_{ped} \approx 0.6$ for ITER ($\kappa \approx 1.7$, $a \approx 2$ m, $L_\parallel \approx 115$ m, $\sin\alpha_u \approx 0.33$). If we use the source width L_s instead of the connection length $L_\parallel$ in the approximation for the parallel loss time (31), we obtain $\Delta R_{SOL}/\Delta R_{ped} \approx 1.8$ for JET (using $L_s \approx 25$ m) and $\Delta R_{SOL}/\Delta R_{ped} \approx 0.9$ for ITER (using $L_s \approx 75$ m).

Although the scaling (19) was derived for convective ELMs, it is interesting that even though parallel conductive losses are difficult to parametrize (figure 21), the total energy losses and also the energy fluence $\epsilon_\parallel$ at the target scale well with pc_st_{ELM} measured in the upstream SOL (midplane, separatrix) both for conductive and convective ELMs (figure 23). This, however, does not strictly reflect the same scaling with pc_st_{ELM} found in the pedestal. Nevertheless, if we adopt the scaling of $\epsilon_\parallel$ with pedestal quantities (19) for conductive ELMs and investigate equation (33) for the other extreme case ($\Delta n_{ped} \approx 0$), the simple approximation of parallel loss time $\tau_\parallel^T$, equation (31), leads to

$$\frac{\Delta R_{SOL}}{\Delta R_{ped}} \approx \frac{1}{0.56} \times \frac{3}{2}\frac{\tau_{pol}}{\tau_\parallel^T}\frac{1}{\sin\alpha_u} \approx \frac{1}{0.56} \times \frac{\pi a\sqrt{\kappa}}{L_\parallel^2 \sin\alpha_u}\frac{\chi_{\parallel,e}}{c_{s,ped}} \quad (36)$$

which is equivalent to the ratio estimated for convective ELMs (35) multiplied by a factor of $\tau_\parallel^n/\tau_\parallel^T$. The approximation (31) for $\tau_\parallel^T$ and consequently the estimate (36) are likely to fail in absolute values. The characteristic parallel particle loss and electron cooling times (31) follow from convective and conductive terms of fluid equations (3)–(6) simplified by replacing gradients by characteristic gradient scales ($\partial/\partial x \approx 1/L_\parallel$). Figure 20 shows that the gradient length for convective

transport can indeed be $L_\parallel$ or better L_s, while temperatures between the target and the source location are quickly equilibrated and $L_\parallel$ underestimates the typical gradient scale for the temperature along the field line. Regardless the absolute values, it is useful to see the functional form of the SOL width $\Delta R_{\rm SOL}$ based on such a simple one-dimensional parallel loss model. The qualitative expression (36) reveals a dependence on the electron collisionality as

$$\frac{\Delta R_{\rm SOL}}{\Delta R_{\rm ped}} \approx \frac{1}{0.56} \times \frac{3.2\pi a\sqrt{\kappa}}{\sqrt{2}L_\parallel \sin\alpha_{\rm u}} \left(\frac{m_{\rm i}}{m_{\rm e}}\right)^{\frac{1}{2}} \frac{1}{\nu^*_{\rm ped}} \tag{37}$$

using the Spitzer–Härm heat diffusivity $\chi_{\parallel,{\rm e}} = 3.2k\,T_{\rm ped}\tau_{\rm e,ped}/m_{\rm e}$ and $\nu^*_{\rm ped} = L_\parallel/v^{\rm e}_{\rm th,ped}\tau_{\rm e,ped}$. Similarly, we obtain an expression

$$\frac{\Delta R_{\rm SOL}}{\Delta R_{\rm ped}} \approx \frac{1}{0.56} \times \frac{3.2\pi a\sqrt{\kappa}}{\sqrt{2}L_\parallel \sin\alpha_{\rm u}} \left(\frac{m_{\rm i}}{m_{\rm e}}\right)^{\frac{1}{2}} \times \frac{1}{\nu^*_{\rm ped}} \left(1 + \frac{3.2}{\alpha_{\rm e}\nu^*_{\rm ped}}\right)^{-1}, \tag{38}$$

if we use a modified heat diffusivity $\chi^{\rm lim}_{\parallel,{\rm e}} = \chi_{\parallel,{\rm e}}(1 + 3.2/\alpha_{\rm e}\nu^*_{\rm ped})^{-1}$ with the electron heat flux limiter $\alpha_{\rm e}$ (in the flux-limited expression for $\chi^{\rm lim}_{\parallel,{\rm e}}$, we again approximated the gradient as $\partial T/\partial x \approx T/L_\parallel$). Quantitatively, the last relation is a strong function of the heat flux limiter $\alpha_{\rm e}$. It gives approximately $\Delta R_{\rm SOL}/\Delta R_{\rm ped} \approx 3.1$ for JET and $\Delta R_{\rm SOL}/\Delta R_{\rm ped} \approx 1.7$ for ITER in the case of $\alpha_{\rm e} = 0.1$ (with the following values used for JET: $\kappa \approx 1.7$, $a \approx 1$ m, $L_\parallel \approx 40$ m, $\sin\alpha_{\rm u} \approx 0.25$, $\nu^*_{\rm ped} \approx 0.1$; and for ITER: $\kappa \approx 1.7$, $a \approx 2$ m, $L_\parallel \approx 115$ m, $\sin\alpha_{\rm u} \approx 0.33$, $\nu^*_{\rm ped} \approx 0.03$), but it is one order of magnitude lower for very strong limiting, $\alpha_{\rm e} = 0.01$, and three orders of magnitude higher without the heat flux limiter, $\alpha_{\rm e} = \infty$.

In the derivation of the relation (35), we assumed that the pedestal density drop is caused by parallel losses, $\Delta n_{\rm ped}/t_{\rm ELM} \approx S^n_\parallel$, equation (29). Similarly in the SOL, we estimated the source (governed by the pedestal losses $\Delta n_{\rm ped}/t_{\rm ELM}$) as $S_n \approx (\partial/\partial x)(nv_\parallel)$, equation (11). This also means that we effectively assume long enough transient so that the solution at the midplane equilibrates, $\partial n/\partial t$ is small compared with the parallel loss term $S^n_\parallel = (\partial/\partial x)(nv_\parallel)$ and the source is balanced by the loss term, $S_n \approx S^n_\parallel$ (see figure 17). Therefore when equating $\Delta W_{\rm ELM}$ lost from the pedestal with $\Delta W_{\rm ELM}$ arriving at the target, $S^n_\parallel$ and S_n cancel. Analogously, if we apply the same to energy, without trying to parametrize the energy source in the SOL, we obtain the same result as (35), no matter what the ratio between convective and conductive losses is. Equation (21) reads as

$$\Delta W_{\rm ELM} \approx 2\pi R\Delta R_{\rm SOL}\sin\alpha_{\rm u} 2\epsilon_\parallel = 4R\Delta R_{\rm SOL}\sin\alpha_{\rm u} t_{\rm ELM} L_{\rm s} S^E_0 \tag{39}$$

and $\epsilon_\parallel$ is related to the energy source in one dimension as $\epsilon_\parallel = \frac{1}{2}t_{\rm ELM}\int S_E {\rm d}x = t_{\rm ELM}L_{\rm s}S^E_0/\pi$ (cosine distribution of the source S_E along the magnetic field with the amplitude S^E_0). In the pedestal,

$$\Delta W_{\rm ELM} \approx \frac{3}{2}\Delta p_{\rm ped} 2\pi a\sqrt{\kappa} 2\pi R\Delta R_{\rm ped} \approx 4\pi^2 Ra\sqrt{\kappa}\Delta R_{\rm ped} t_{\rm ELM} S^E_\parallel \tag{40}$$

where we used

$$\frac{\rm d}{{\rm d}t}\left(\frac{3}{2}p_{\rm ped}\right) \approx \frac{3}{2}\frac{\Delta p_{\rm ped}}{t_{\rm ELM}} \approx S^E_\parallel, \tag{41}$$

analogously to equation (29). If the energy loss from the pedestal during the ELM crash translates to the energy source in the SOL, from equating $S^E_\parallel$ in (41) to S^E_0, we obtain

$$\frac{\Delta R_{\rm SOL}}{\Delta R_{\rm ped}} \approx \frac{\pi^2 a\sqrt{\kappa}}{L_{\rm s}\sin\alpha_{\rm u}}, \tag{42}$$

i.e. the same as (35) where $3A/2\pi \approx 0.56$, A is defined in (12) ($A \approx 1$), and where $L_\parallel$ was used in (30) instead of $L_{\rm s}$. The relation (42) is the result of a simple model equating pedestal energy losses to parallel loss factors in one-dimensional picture.

References

[1] Havlíčková E *et al* 2011 *J. Nucl. Mater.* **415** S471
[2] Wiesen S *et al* 2011 *Plasma Phys. Control. Fusion* **53** 124039
[3] Pitts R A *et al* 2007 *Nucl. Fusion* **47** 1437
[4] Thomsen H *et al* 2010 *Proc. 23rd IAEA Fusion Energy Conf. (Daejeon, Korea)* EXD/6-6Rb
[5] Eich T *et al* 2011 *J. Nucl. Mater.* **415** S856
[6] Fundamenski W *et al* 2011 *Nucl. Fusion* **51** 083028
[7] Gulejová B 2010 *SOLPS Modelling of ELMing H-mode PhD Thesis* EPFL Lausanne
[8] Lönnroth J S *et al* 2006 *Contrib. Plasma Phys.* **46** 726
[9] Havlíčková E *et al* 2011 *Plasma Phys. Control. Fusion* **53** 065004
[10] Bergmann A 2002 *Nucl. Fusion* **42** 1162
[11] Tskhakaya D *et al* 2007 *Proc. 34th EPS Conf. on Plasma Phys. (Warsaw, Poland)* vol 31F O-2.002
[12] Tskhakaya D *et al* 2009 *J. Nucl. Mater.* **390-391** 335
[13] Tskhakaya D *et al* 2007 *Contrib. Plasma Phys.* **47** 563
[14] Tskhakaya D *et al* 2007 *J. Comput. Phys.* **225** 829
[15] Tskhakaya D *et al* 2008 *Contrib. Plasma Phys.* **48** 121
[16] Tskhakaya D *et al* 2011 *J. Nucl. Mater.* **415** S860
[17] Tskhakaya D *et al* 2008 *Contrib. Plasma Phys.* **48** 89
[18] Manfredi G *et al* 2011 *Plasma Phys. Control. Fusion* **53** 015012
[19] Filbet F *et al* 2001 *J. Comput. Phys.* **172** 166
[20] Crispel P *et al* 2007 *J. Comput. Phys.* **223** 208
[21] Pamela S 2011 *Plasma Phys. Control. Fusion* **53** 054014
[22] Loarte *et al* 2002 *Plasma Phys. Control. Fusion* **44** 1815
[23] Manfredi G *et al* 2011 *38th EPS Conf. on Plasma Phys. (Strasbourg, France)*
[24] Fundamenski W and Pitts R A 2006 *Plasma Phys. Control. Fusion* **48** 109
[25] Eich T *et al* 2009 *J. Nucl. Mater.* **390-391** 760
[26] Moulton D 2011 Plasma exhaust modelling of h-mode discharges on JET *PhD Thesis* Imperial College London submitted
[27] Loarte *et al* 2008 *22nd IAEA Fusion Energy Conf. (Geneva, Switzerland)*
[28] Beurskens M N A *et al* 2009 *Nucl. Fusion* **49** 125006
[29] Fundamenski W 2010 *Power Exhaust in Fusion Plasmas* (Cambridge: Cambridge University Press)
[30] Loarte *et al* 2000 *18th IAEA Fusion Energy Conf. (Sorrento, Italy)*